Article

SARS-CoV-2 Envelope Protein Forms Clustered Pentamers in Lipid Bilayers

Noah H. Somberg, Westley W. Wu, João Medeiros-Silva, Aurelio J. Dregni, Hyunil Jo, William F. DeGrado, and Mei Hong*

Cite This: *Biochemistry* 2022, 61, 2280−2294

Read Online

ACCESS | Metrics & More | Article Recommendations | Supporting Information

ABSTRACT: The SARS-CoV-2 envelope (E) protein is a viroporin associated with the acute respiratory symptoms of COVID-19. E forms cation-selective ion channels that assemble in the lipid membrane of the endoplasmic reticulum Golgi intermediate compartment. The channel activity of E is linked to the inflammatory response of the host cell to the virus. Like many viroporins, E is thought to oligomerize with a well-defined stoichiometry. However, attempts to determine the E stoichiometry have led to inconclusive results and suggested mixtures of oligomers whose exact nature might vary with the detergent used. Here, we employ ^{19}F solid-state nuclear magnetic resonance and the centerband-only detection of exchange (CODEX) technique to determine the oligomeric number of E's transmembrane domain (ETM) in lipid bilayers. The CODEX equilibrium value, which corresponds to the inverse of the oligomeric number, indicates that ETM assembles into pentamers in lipid bilayers, without any detectable fraction of low-molecular-weight oligomers. Unexpectedly, at high peptide concentrations and in the presence of the lipid phosphatidylinositol, the CODEX data indicate that more than five ^{19}F spins are within a detectable distance of about 2 nm, suggesting that the ETM pentamers cluster in the lipid bilayer. Monte Carlo simulations that take into account peptide−peptide and peptide−lipid interactions yielded pentamer clusters that reproduced the CODEX data. This supramolecular organization is likely important for E-mediated virus assembly and budding and for the channel function of the protein.
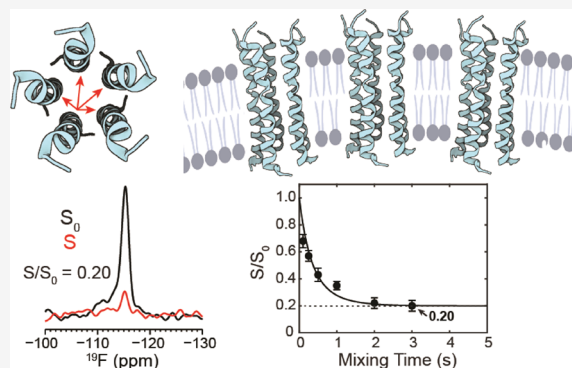
INTRODUCTION

Severe acute respiratory syndrome coronavirus 2 (SARS-CoV-2), the causative agent of the COVID-19 pandemic, encodes three membrane proteins: the spike protein (S), the matrix protein (M), and the envelope protein (E).[1] The vaccine-targeted spike protein mediates entry of the virus into the host cell, while the matrix protein organizes the assembly of new virus particles in the endoplasmic reticulum Golgi intermediate compartment (ERGIC) of the cell. The envelope protein, the least understood among the three proteins, assists in the assembly and budding of the virus and functions as a cation channel.[2,3] The channel activity of E in SARS-CoV-1 is not essential for the virus localization to the ERGIC or the production of new virus particles in cell cultures. However, lack of E channel activity reduced viral fitness and deletion of E gave rise to attenuated viruses in animal models.[4] Transient expression of the E protein of SARS-CoV-2 is sufficient to induce in vitro death in human bronchial and alveolar basal epithelial cell lines.[5] Moreover, injection of E alone into mice provokes strong immune responses and causes acute respiratory distress symptoms that damage the lungs and spleen, similar to that seen in human COVID-19 patients. In

mice infected with SARS-CoV-2, the administration of E inhibitors significantly attenuated inflammation and production of viral particles.[5] Therefore, E is a potential antiviral drug target to ameliorate the respiratory symptoms of COVID-19.[6]

To develop E inhibitors as antiviral drugs, atomic-resolution structural information of the protein is essential.[7] We recently determined the high-resolution structure of the E transmembrane domain (ETM) (Figure 1a) in lipid bilayers using solid-state nuclear magnetic resonance (ssNMR) spectroscopy.[8] In lipid mixtures that mimic the ERGIC membrane and under ionic conditions that produce the closed state of the channel, the ETM exhibits well-resolved ssNMR spectra. Measured chemical shifts and interhelical distance constraints allowed determination of the conformation and interhelical packing of the protein.[8] In solving this closed-state structure,
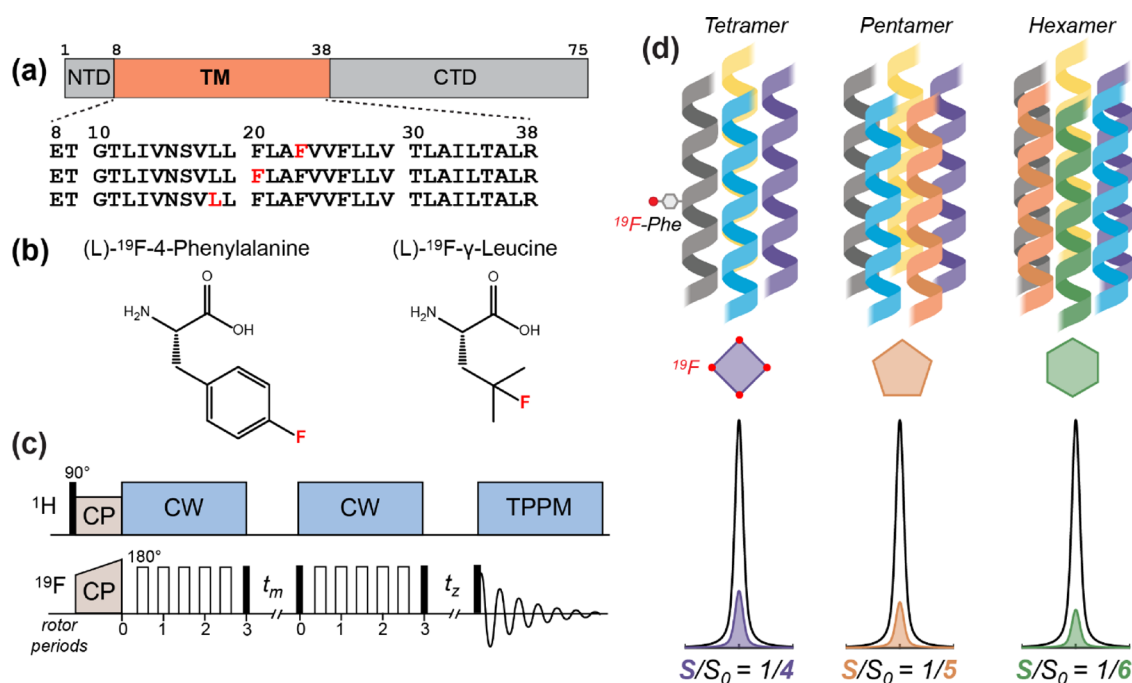
Figure 1. ^{19}F solid-state NMR approach for determining the stoichiometry of ETM assembly in lipid bilayers. (a) Amino acid sequence diagram of the SARS-CoV-2 E protein. The transmembrane (TM) domain is preceded by a short N-terminal domain (NTD) and is followed by a C-terminal domain (CTD). The amino acid sequences of singly fluorinated ETM peptides used in this study are shown. (b) Structures of the 4-^{19}F-phenylalanine and ^{19}F-Cγ-leucine that are synthetically incorporated into the ETM peptide. (c) Pulse sequence of the ^{19}F CODEX experiment. Filled and open rectangles denote 90 and 180° pulses, respectively. CP: cross-polarization; CW continuous-wave heteronuclear decoupling; TPPM, two-phase modulation heteronuclear decoupling. ^{19}F spin diffusion during the mixing time t_m reduces the intensity of a ^{19}F spin echo. The CODEX dephased (S) experiment has a long t_m and a short t_z, while the CODEX control (S_0) experiment has a short t_m and a long t_z. The sum of the two mixing times is the same between S and S_0. (d) Schematic of different stoichiometries of the ETM oligomer in the lipid membrane, with corresponding relative intensities of the CODEX S_0 and S spectra.

we assumed that the ETM assembles into five-helix bundles in the lipid bilayer. This assumption was based on previous gel electrophoresis and analytical ultracentrifugation (AUC) data of the SARS-CoV-1 E protein.[9−11] However, the stoichiometry of the ETM oligomer is so far still inconclusive. Most gel electrophoresis data show multiple bands, many of which are not well resolved. The largest oligomer number observed in these gels depends on the choice of the detergent, the E protein construct length, and the presence or absence of cysteines and reducing agents. Sodium dodecyl sulfate polyacrylamide gel electrophoresis (SDS-PAGE) promotes low-molecular-weight (MW) oligomers such as dimers and trimers,[9,11] while neutral detergents such as dodecylphosphocholine (DPC), perfluorooctanoic acid, and C14 betaine promote larger oligomers. These biophysical assays used three construct lengths of the SARS-CoV-1 E protein—ETM (8−38),[10] ETR (8−65),[9] and full-length E (EFL). ETR includes the TM domain and a portion of the cytoplasmic domain and is thus an intermediate construct between the ETM and EFL.[11] The TM amino acid sequences of SARS-CoV-1 and the original isolate of SARS-CoV-2 E proteins are identical, while the cytoplasmic domains of the two proteins have only four mutations: T55S, V56F, E69R, and G69Δ. Among the three constructs, the ETM yielded the best resolved bands in gel electrophoresis data but still showed a distribution of oligomeric states that varies among different detergents.[10,12] AUC experiments similarly suggest variable oligomeric states. The radial distribution profile of the DPC-bound ETM is best fit to a monomer−pentamer equilibrium, while SDS/DPC-bound ETR exhibits a mixture of tetramers and pentamers.

Compared to the ETM, EFL exhibits a pentameric state only under reducing conditions.

In addition to SARS-CoV-1 E, the oligomeric structure of the E protein of two other coronaviruses has been investigated experimentally. The Middle East respiratory symptom (MERS)-CoV full-length E was studied in DPC, 1,2-diheptanoylglycerophosphocholine, and lyso-myristoylphosphatidylcholine detergents. In analogy to SARS-CoV-1 E, gel electrophoresis data showed a continuum of bands that suggest, but do not definitively determine, a pentameric state for MERS-CoV E.[13] AUC data of the protein in C14-betaine micelles provide clearer indications of a pentameric state. The avian infectious bronchitis virus (IBV) E protein was investigated using sucrose gradient analysis and other biochemical experiments.[14] The data show that IBV E exists in a low MW pool and a high MW pool in both transfected and infected cells. The low MW component is either monomeric or dimeric, while the high MW component is pentameric or hexameric. Importantly, the majority of virion-associated IBV E protein is found in the high MW pool, and production of virus-like particles (VLPs) required the high MW E oligomers. Mutations of key TM residues in the IBV E shifted the populations of the two MW components, affected VLP production, altered the secretory pathway function of the protein, and changed the membrane topology of the protein.[15] These results suggest that different oligomeric states of the IBV E may carry out different functions. The potential coexistence of multiple oligomeric states of the E proteins of SARS-CoV-1 and IBV was also suggested by early global search molecular dynamics simulations of E proteins from 13 coronaviruses.[12]

These in vacuo simulations searched for common low-energy helix orientation, helical bundle handedness, and oligomeric sizes. The results suggested that the ETM of SARS-CoV-1 and other coronaviruses may adopt a mixture of dimers, trimers, and pentamers.

This survey shows that the oligomeric state of coronavirus E proteins has not been convincingly established, despite efforts in the last two decades. Furthermore, none of the biophysical measurements to date have been conducted in lipid bilayers. Protein stoichiometry in lipid bilayers is a key aspect of the structure and function of membrane proteins. Most membrane proteins oligomerize with well-defined stoichiometries. Mammalian ion channels are dominated by tetrameric helical bundles, while viral fusion proteins are predominantly trimeric. Among viroporins, the influenza M2 proton channel is tetrameric, as established by channel activity data,[16] biophysical AUC data,[17,18] ^{19}F solid-state NMR data in lipid bilayers,[19,20] and X-ray crystal structures in detergents[21] and lipid cubic phases.[22] In comparison, the HIV viral protein U (Vpu) assembles into a pentameric cation channel.[23−26]

To elucidate the oligomeric state of the SARS-CoV-2 E protein in lipid bilayers and to ascertain if the protein might adopt two distinctly different oligomeric states, here we apply ^{19}F solid-state NMR spectroscopy to fluorinated ETM peptides in lipid bilayers. Specifically, we employ the centerband-only detection of exchange (CODEX) technique, which allows counting of the number of ^{19}F spins within a distance of about 2 nm.[19,27−30] We synthesized singly fluorinated ETM peptides and reconstituted them into ERGIC-mimetic lipid bilayers and several other simplified lipid membranes. We show that ETM assembles into pentamers in all lipid compositions studied. Unexpectedly, we discovered that these ETM pentamers cluster in membranes that contain phosphatidylinositol, whose derivatives are involved in intracellular signaling. This suggests a possible mechanism with which interactions between E and viral and host membrane proteins may play a role in the pathogenic activities of the virus.

■ MATERIALS AND METHODS

Synthesis of 4-^{19}F-Phe-Labeled ETM Peptides. The TM domain of the SARS-CoV-2 E protein spanning residues 8−38 and containing a 4-^{19}F-Phe23 label was produced by Fmoc solid-phase peptide synthesis. The amino acid sequence is ETG TLIVNSVLLF LAFVVFLLVT LAILTALR-NH$_2$. We used a custom-built fast-flow synthesizer that achieves each coupling in 3 min per residue.[31] H-Rink amide ChemMatrix resin at a 0.10 mmol scale (0.20 g at 0.5 mmol/g loading size) was loaded into the reactor, which was kept at 70 °C using a water bath. Each amino acid was coupled in 10-fold excess (1.0 mmol). The Fmoc-amide and side chain protected amino acids were dissolved in hexafluorophosphate azabenzotriazole tetramethyl uronium (HATU) solution (2.5 mL per residue, 0.38 M HATU in dimethylformamide (DMF) solution, 9.5 equiv). For each amino acid coupling, diisopropylethylamine (DIPEA, 348 μL, 2.0 mmol, 20 equiv) was added to the vial, and the amino acids were delivered via a syringe pump (3.9 mL/min, 45 s). The coupling was followed by a wash with DMF (20 mL/min, 55 s) delivered using a high-pressure liquid chromatography (HPLC) pump. Each residue was deprotected with a DMF solution containing 20% piperidine (20 mL/min, 25 s), followed by a DMF wash (20 mL/min, 65 s) to remove residual piperidine. After the final amino acid coupling, the solvent was flushed from the reactor, and the resin was washed

three times with dichloromethane and then dried under room temperature (RT) vacuum overnight. The following day the peptide was deprotected and cleaved from the resin using 5 mL of trifluoroacetic acid/phenol/water/triisopropylsilane solution (88:5:5:2 by volume), shaking for 2 h at RT. The resin was filtered off, and the crude peptide was precipitated from the cleavage solution with cold diethyl ether and then washed twice with cold diethyl ether before being dried under house vacuum (50 mBar, RT) overnight. The resulting crude peptide was dissolved in trifluoroethanol and purified by preparative reverse-phase HPLC using a Vydac C4 column (22 mm × 250 mm, 10 μm particle size) and a linear gradient of 80−100% methanol (with the remaining fraction water) over 25 min at a flow rate of 10 mL/min. The peptide was eluted at ~99% methanol. Fractions containing the peptide were assessed for relative purity by MALDI mass spectrometry (Figure S1) (observed m/z: 3381.0, calculated m/z: 3378.2) and concentrated under reduced pressure on a rotary evaporator, followed by lyophilization. About 20 mg of purified peptide was obtained as a white powder from the 0.10 mmol synthesis scale, corresponding to an overall yield of ~5%.

Synthesis of γ-^{19}F-Leu18-Labeled ETM. Fmoc-4-fluoroleucine was synthesized from commercially available 2(S)-amino-4-fluoro-4-methylpentanoic acid using typical Fmoc protection conditions[32] for amino acid (FmocOsu, NaHCO$_3$ in H$_2$O−acetone). The C−F group is installed on the Cγ carbon of the amino acid; thus, in the rest of the paper, we designate this residue as γ-^{19}F-Leu. An ETM peptide (residues 8−38) containing γ-^{19}F-Leu at residue 18 (Ac-ETG TLIVNSVL$_{γ-F}$LF LAFVVFLLVT LAILTALR-NH$_2$) was synthesized on TantaGel S Ram resin (0.25 mmol/g, 0.1 mmol scale) using an automated microwave peptide synthesizer (Biotage Alstra + Initiator). The deprotection step was carried out for 5 min at 70 °C with 20% 4-methylpiperidine in DMF (4.5 mL), and each coupling step was done twice for 5 min at 75 °C with Fmoc-protected amino acids (5 equiv), HCTU (4.98 equiv), and DIPEA (10 equiv) in DMF at a final concentration of 0.125 M amino acids. The N-terminus of the peptide was acetylated using Ac$_2$O (10 equiv) and DIPEA (20 equiv) in DMF for 1 h at RT. The peptide was cleaved from the resin by 3-h treatment with a 95% TFA solution (10 mL) containing 2.5% TIPS and 2.5% water. The crude peptide was obtained by blowing off TFA using nitrogen gas, followed by precipitation with cold diethyl ether. The crude peptide was purified by RP-HPLC (C4 Vydac column, mobile phase A: 0.1% TFA in H$_2$O, B: 0.1% TFA in i-PrOH/CH$_3$CN/H$_2$O (60/30/10), flow rate: 10 mL/min, gradient: 60−100% B over 40 min). Analytical HPLC and MALDI (observed m/z: 3421.75, calculated m/z: 3421.15 for MH$^+$($C_{165}H_{274}N_{36}O_{40}F^+$)) confirmed the chemical entity and purity.

Preparation of Proteoliposomes. To reconstitute the ETM into lipid bilayers, the purified peptide was dissolved in methanol at 1 mg/mL and dry lipids in chloroform at a total concentration of 15 mg/mL. The peptide solution was added to the lipid solution, and then, the bulk organic solvent was removed with a stream of nitrogen gas (RT, 1 h). Residual organic solvent was further removed under house vacuum (50 mBar, RT, 4 h), followed by lyophilization overnight. The dry proteoliposome film was resuspended in 3 mL of pH 7.5 Tris buffer (25 mM tris, 25 mM NaCl, 1 mM EDTA, 0.07 mM NaN$_3$), vortexed, and sonicated five times, five seconds each. The proteoliposome solution was incubated for 1 h at RT, with

gentle agitation every 10 min. The homogeneous solution was then frozen in liquid nitrogen until solid (90 s) and thawed in a 42 °C water bath until warmed (4 min). This freeze−thaw cycle was repeated 8 times total to produce multilamellar vesicles. The homogeneous opaque white proteoliposome solution was ultracentrifuged at $311{,}000 \times g$ at 10 °C for 4 h to obtain an opaque off-white membrane pellet. The wet pellet was dried in a desiccator at RT until the sample reached a hydration level of ∼40% (w/w) of the total mass of protein, lipid, and water, $m_{water}/(m_{water} + m_{protein} + m_{lipid}) \approx 40\%$. The pellet was packed into a 1.9 mm Bruker MAS rotor at $5000 \times g$ with a benchtop Beckman Coulter swinging-bucket rotor.

To investigate the effect of the lipid composition on the supramolecular organization of ETM, we reconstituted the ETM into four membrane mixtures. The main lipid mixture is an ERGIC mimetic membrane,[33−35] composed of 1-palmitoyl-2-oleoyl-glycero-3-phosphocholine (16:0−18:1 PC; POPC), 1-palmitoyl-2-oleoyl-sn-glycero-3-phosphoethanolamine (16:0−18:1 PE; POPE), L-α-phosphatidylinositol (liver, bovine; PI), 1-palmitoyl-2-oleoyl-sn-glycero-3-phospho-L-serine (16:0−18:1 PS; POPS), and cholesterol (chol). All lipids were purchased from Avanti Polar Lipids without further purification. The molar ratios of POPC:POPE:PI:POPS:Chol in this ERGIC membrane are 9:4:2.6:1.4:3. Three ERGIC membrane samples with different peptide (monomer) to phospholipid (P:L) molar ratios of 1:8.5, 1:17, and 1:34 were prepared. Cholesterol is not considered in the peptide to phospholipid ratios, and cholesterol concentrations are presented separately. We also prepared two simplified ERGIC-like membranes. The first membrane omits cholesterol and thus has a molar composition of POPC:POPE:PI:POPS = 9:4:2.6:1.4. The P:L molar ratio was 1:17. The second membrane omits cholesterol and phosphatidylinositol. The POPC:POPE:POPS molar ratios were 9:4:1.4, while the P:L molar ratio was 1:17. Finally, we prepared a model membrane containing 1,2-dimyristoyl-sn-glycero-3-phosphocholine (14:0 PC, DMPC) and 1,2-dimyristoyl-sn-glycero-3-phospho-(1′-rac-glycerol) (14:0 PG, DMPG) at a molar ratio of 7:3. The P:L molar ratio for this sample was 1:30.

Solid-State NMR Spectroscopy. ^{19}F solid-state NMR experiments were conducted with an Avance III HD 600 MHz [1]H (14.1 T) spectrometer using a Bruker 1.9 mm HFX magic-angle spinning (MAS) probe. Additional ^{19}F solid-state NMR experiments were conducted with an Avance III HD 400 MHz [1]H (9.4 T) spectrometer using a Bruker 4 mm HFX probe for ^{19}F experiments. All ^{19}F externally referenced to 5-^{19}F-trptophan at −122.1 ppm on the CF_3Cl scale. Typical radiofrequency field strengths were 50−80 kHz for ^{1}H and 50−62 kHz for [19]F.

[19]F CODEX experiments were conducted at 18 kHz MAS at thermocouple reported temperatures of 240−244 K. Typical sample heating at 18 kHz MAS results in a sample temperature of 2−4 K greater than thermocouple reported temperatures. A ^{1}H excitation pulse of 71.4 kHz was used, followed by cross-polarization (CP) for 750 μs under the sideband matching condition of $\omega_{1,H}$ (80 kHz) − $\omega_{1,F}$ (62 kHz) = ω_r (18 kHz). A linear 70−100% ramp was used on the ^{19}F spin-lock pulse. This [1]H-^{19}F CP was followed by a short (1 ms) pre-trigger z-filter for rotor synchronization. Two rotor-synchronized 180°-pulse trains recouple the ^{19}F chemical shift anisotropy (CSA) under MAS. Three 180°-pulses were used in each pulse train, giving a CSA recoupling time of $2\tau_r = 0.11$ ms per pulse train.

The two CSA recoupling periods sandwich the mixing time t_m, during which no pulses or decoupling was applied. The mixing time was rotor synchronized with triggering on the second 90° pulse. To correct for spin−lattice relaxation during the mixing time, we added a z-filter (t_z) after the second 180°-pulse train. The CODEX experiment was run in pairs. The exchange experiment (S) was run with the desired t_m first and a short (10 μs) t_z period second, while the control experiment (S_0) was run with the short t_z period first and the long mixing period second. The normalized integrated intensity, S/S_0, of the centerband is reported for each mixing time.

NMR Spectral Analysis. All MAS NMR spectra were processed using TopSpin 3.6. Typical spectra were processed using Gaussian apodization with LB = −40 Hz and GB = 0.02. For ^{19}F-Phe23 spectra, S/S_0 values were obtained from integration of the centerband (−100 to −125 ppm). The error bar σ on the S/S_0 values was estimated based on the signal-to-noise ratio (SNR) of the spectra using $\sigma = (S/S_0)[(SNR_{S_0}^{-2} + SNR_S^{-2})^{1/2}]$.

Simulation of CODEX Data Using Random Distribution and Clustered Distribution. The CODEX decay curves of multiple oligomers were simulated by first computing the number of oligomers N expected in a 100×100 nm^2 square based on the area of the channel, assuming circular channels of radius r, an oligomeric number of n, a peptide monomer to lipid molar ratio P, and the lipid head group area A_L. All simulations use a lipid head group area $A_L = 60$ Å^2 based on existing measurements of lipid structural parameters:[36,37]

$$N = \frac{10^6 \text{ Å}^2}{A_L n \frac{P}{2} + \pi r^2} \tag{1}$$

A random spatial arrangement of oligomers was produced using the random sequential adsorption (RSA) method implemented in MATLAB (Supporting Information).[38] Two pseudorandom numbers (with uniform probability distribution) were generated in the interval [0, 1000]. The center of each oligomer was placed at the x−y coordinate that corresponds to the two randomly generated numbers. If the position of an oligomer overlaps with the previously generated oligomer within the radius of the channel, then the oligomer was rejected. This was repeated N times to generate the positions of the oligomers. A channel radius of 12.8 Å was chosen to match the excluded volume of the cylindrical channel in the clustered distribution.

To generate a clustered distribution of oligomers, we started N oligomers distributed randomly on a 100×100 nm^2 square. Oligomers were initially allowed to overlap within their 12.8 Å, as the interaction potential was used to exclude oligomer overlap. The potential of mean force used was constructed based on a pairwise cylinder−cylinder interaction potential for a positive hydrophobic mismatch of 1 nm.[39] This mismatch was chosen based on an approximate length of 4 nm for the hydrophobic domain of the ETM[8] and an approximate hydrophobic thickness of 3 nm for a POPC bilayer.[36] Numerical values for the potential are provided in the Supporting Information. The position of each oligomer was adjusted according to this positive-mismatch potential using an implementation of the Metropolis Monte Carlo method.[40] Specifically, a random pore was selected and its total pairwise interaction energy to every other pore, E_i, was calculated under periodic boundary conditions on the 100×100 nm^2 square.

Table 1. Membrane Compositions, CODEX Intensities at the Longest Mixing Times, and Best-Fit Parameters of 4-^{19}F-Phe23-Labeled ETM

lipid and molar composition	P:L	^{19}F T_1 (s)	S/S$_0$	S$_0$/S	r (Å)
ERGIC: POPC/POPE/PI/POPS/Chol (9:4:2.6:1.4:3)	1:17	4.5	0.14 ± 0.03	7.1	8.8
ERGIC	1:34	3.2	0.20 ± 0.04	5.0	8.7
ERGIC	1:8.5	4.1	0.16 ± 0.03	6.3	8.6
POPC/POPE/PI/POPS (9:4:2.6:1.4)	1:17	4.1	0.17 ± 0.02	5.9	8.4
POPC/POPE/POPS (9:4:1.4)	1:17	0.9	0.22 ± 0.06	4.2	8.4
DMPC/DMPG (7:3)	1:30	1.5	0.21 ± 0.04	4.8	8.0

The pore was then randomly moved to a new position, and the total pairwise interaction energy of the pore in the new position with all other pores, E_f, was computed. If $E_f \leq E_i$, then the new position was accepted. If $E_f > E_i$, then according to the detailed balance, the new position was accepted with probability $\exp(E_i - E_f)$ where E_i and E_f are in units of $k_B T$. After the new position was either accepted or rejected, a new pore was randomly selected starting from the final state of the previous move. This process was repeated for 50,000 iterations. The average nearest-neighbor distance between oligomers was monitored and was not observed to change significantly after approximately 10,000 iterations.

After the N pore positions were generated using either RSA or the Monte Carlo method based on the cylinder−cylinder interaction potential, each oligomer was placed as a regular polygon of n vertices with side length r. Each polygon was given a random rotation around its center in the bilayer plane. A distance matrix of dimensions $(N \times n) \times (N \times n)$ was constructed to account for all inter- and intra-oligomer ^{19}F−^{19}F distances. In constructing the distance matrix, boundary effects are assumed to be negligible, and hard-wall boundary conditions are used. Total ^{19}F−^{19}F dipolar coupling converges after summing over approximately a 20 Å radius, including all couplings greater than 12 Hz. Thus, to increase computational efficiency, all distances greater than 50 Å, which correspond to ^{19}F−^{19}F dipolar couplings of less than 0.85 Hz, were neglected. CODEX intensities were then calculated as described previously[19] to produce mixing-time dependent decay curves.

■ RESULTS

SARS-CoV-2 ETM Forms Pentamers in Lipid Bilayers. To investigate the oligomeric state of SARS-CoV-2 E, we synthetized three singly fluorinated ETM peptides (Figure 1a). 4-^{19}F-Phe23-labeled ETM was the primary construct for the majority of the ^{19}F CODEX experiments presented here, while 4-^{19}F-Phe20-labeled ETM and γ-^{19}F-Leu18-labeled ETM provided additional support (Figure 1b). Because the protein localizes to the ERGIC membrane during the SARS-CoV-2 virus lifecycle,[41,42] we reconstituted the ETM into an ERGIC-mimetic lipid bilayer containing POPC, POPE, POPS, PI, and cholesterol (Table 1). To ascertain whether certain lipids in this mixture significantly impact the oligomeric structure, we also prepared simplified membrane mixtures utilizing fewer lipid components.

We use the ^{19}F CODEX technique[19,28] to determine the oligomeric number of ETM. This technique measures the intensity of a ^{19}F spin echo after spin polarization transfer during a mixing time t_m (Figure 1c). When several ^{19}F spins with different chemical shift tensor orientations are within ~2 nm of each other, polarization transfer among them mediated by ^{19}F−^{19}F dipolar couplings decreases the CODEX echo

intensity. This reduced echo intensity results in an intensity ratio of less than 1 between a dephased experiment, S, and a control experiment, S$_0$. The control experiment was conducted to account for T_1 relaxation during the mixing time. At sufficiently long mixing times when the magnetization is equilibrated among the n spins of an n-oligomer, the CODEX intensity decreases to 1/n, which corresponds to the fraction of magnetization that resides on the source spin with the initial orientation. Thus, a dimer should result in a CODEX equilibrium S/S$_0$ value of 1/2, a trimer 1/3, a tetramer 1/4, and so on (Figure 1d).

^{19}F chemical shift is highly sensitive to the local electronic environment of the fluorine atom and is therefore sensitive to the molecular structure. One-dimensional ^{19}F CP and direct-polarization spectra of 4-^{19}F-Phe23-labeled ETM show a dominant peak at −115 ppm (Figure 2a), indicating a homogeneous sidechain conformation. Some of the membrane samples also exhibit a minor peak at −111 ppm, whose intensity accounts for 5−25% of the total spectral intensity. The simplicity of these spectra facilitates the determination of the oligomeric state of the ETM using CODEX.

We first measured the CODEX spectra of 4-^{19}F-Phe23-labeled ETM bound to the ERGIC membrane (Figure 2b). At a P:L of 1:17, the T_1-corrected CODEX intensities, S/S$_0$, decayed to 0.19 ± 0.02 at a mixing time of 3 s (Figure 3a, Table 2), suggesting a pentamer. This low S/S$_0$ value excludes the presence of a substantial fraction of small oligomers such as monomers, dimers, or trimers, as they would contribute much higher CODEX intensities of 1, 0.5, and 0.33.

The 3 s CODEX mixing time is the longest documented so far in the literature.[19,20,27,43−46] By this mixing time, all viral and bacterial membrane proteins that have been studied so far using this experiment have equilibrated their intensities. However, the intensities of the 1:17 ETM sample at 2 and 3 s are not yet equilibrated. To measure the equilibrium value that would confirm the oligomeric number, we increased the mixing time further to 4 s. This 4 s CODEX experiment was enabled by the unusually long ^{19}F T_1 relaxation time of 4.5 s for this ERGIC-bound ETM at this concentration. To our surprise, the 4 s CODEX S/S$_0$ value is even lower, at 0.14 ± 0.03, which would suggest a heptamer (n = 7). However, the continuing drop of the CODEX intensities gives a non-exponential shape to the decay curve, suggesting additional magnetization transfer beyond that of an isolated oligomer. Since the 1:17 sample also has a long ^{19}F T_1, we hypothesized that multiple ETM oligomers might be clustered in the membrane at this peptide concentration. This clustering both rigidifies the aromatic sidechains, thus slowing down ^{19}F T_1 relaxation, and at the same time causes interoligomer contacts that accelerate CODEX dephasing at long mixing times. To test this hypothesis, we prepared a twofold diluted sample with a P:L of 1:34. The ^{19}F spectra of this sample (Figure 2a,c) are
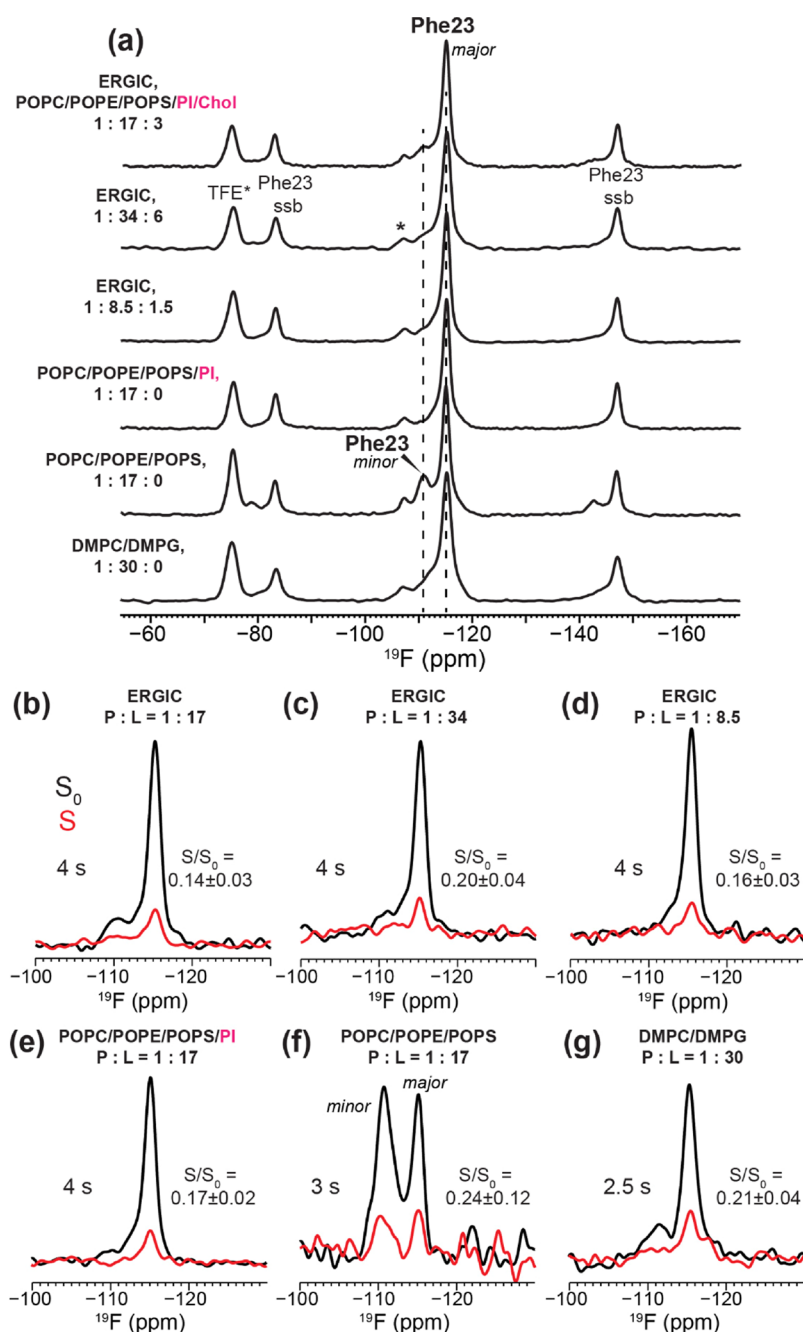
Figure 2. Representative ¹⁹F NMR spectra of 4-¹⁹F-Phe23-labeled ETM in different lipid membranes. All spectra were measured at a thermocouple reported temperature of 240−244 K and 18 kHz MAS. (a) ¹⁹F CP spectra of the six membrane-bound ETM samples. For all membranes the peptide (monomer)/phospholipid/cholesterol ratios are specified. (b−g) CODEX control S_0 (black) and dephased S (red) spectra of the ETM at selected mixing times. (b) 4 s CODEX spectra of the ERGIC-bound ETM at P:L = 1:17. (c) 3 s CODEX spectra of the ERGIC-bound ETM at P:L = 1:34. (d) 4 s CODEX spectra of the ERGIC-bound ETM at P:L = 1:8.5. (e) 4 s CODEX spectra of the ETM bound to the cholesterol-free ERGIC membrane at P:L = 1:17. (f) 3 s CODEX spectra of the ETM bound to the POPC/POPE/POPS membrane at P:L = 1:17. The peak doubling indicates the presence of two Phe23 sidechain conformations in this membrane. (g) 2.5 s CODEX spectra of the ETM in the DMPC/DMPG membrane at P:L = 1:30. The S/S_0 values based on the integrated intensities of these CODEX spectra are given in (b−f).

unchanged from the 1:17 sample, but its CODEX intensities now plateau clearly between 2 and 3 s to an S/S_0 value of 0.20 ± 0.04 (Figure 3b), indicating a pentamer. These data demonstrate that individual ETM channels are pentameric in ERGIC-mimetic lipid bilayers, and these pentamers cluster at high peptide concentrations. Consistent with the equilibration of the CODEX intensities at the lower peptide concentration, the sample also exhibits a shorter ¹⁹F T_1 relaxation time of 3.2

s, indicating that the Phe23 sidechain is more dynamic when ETM channels are better separated.

To further verify that multiple ETM pentamers indeed cluster at high peptide concentrations, we prepared a third ERGIC-bound protein sample with a P:L of 1:8.5. Compared to the 1:17 sample, this highest concentration protein sample displays a similar CODEX intensity of 0.16 ± 0.03 at the longest mixing time of 4 s, but at shorter mixing times, the intensities are lower than those of the 1:17 sample (Figures 2d
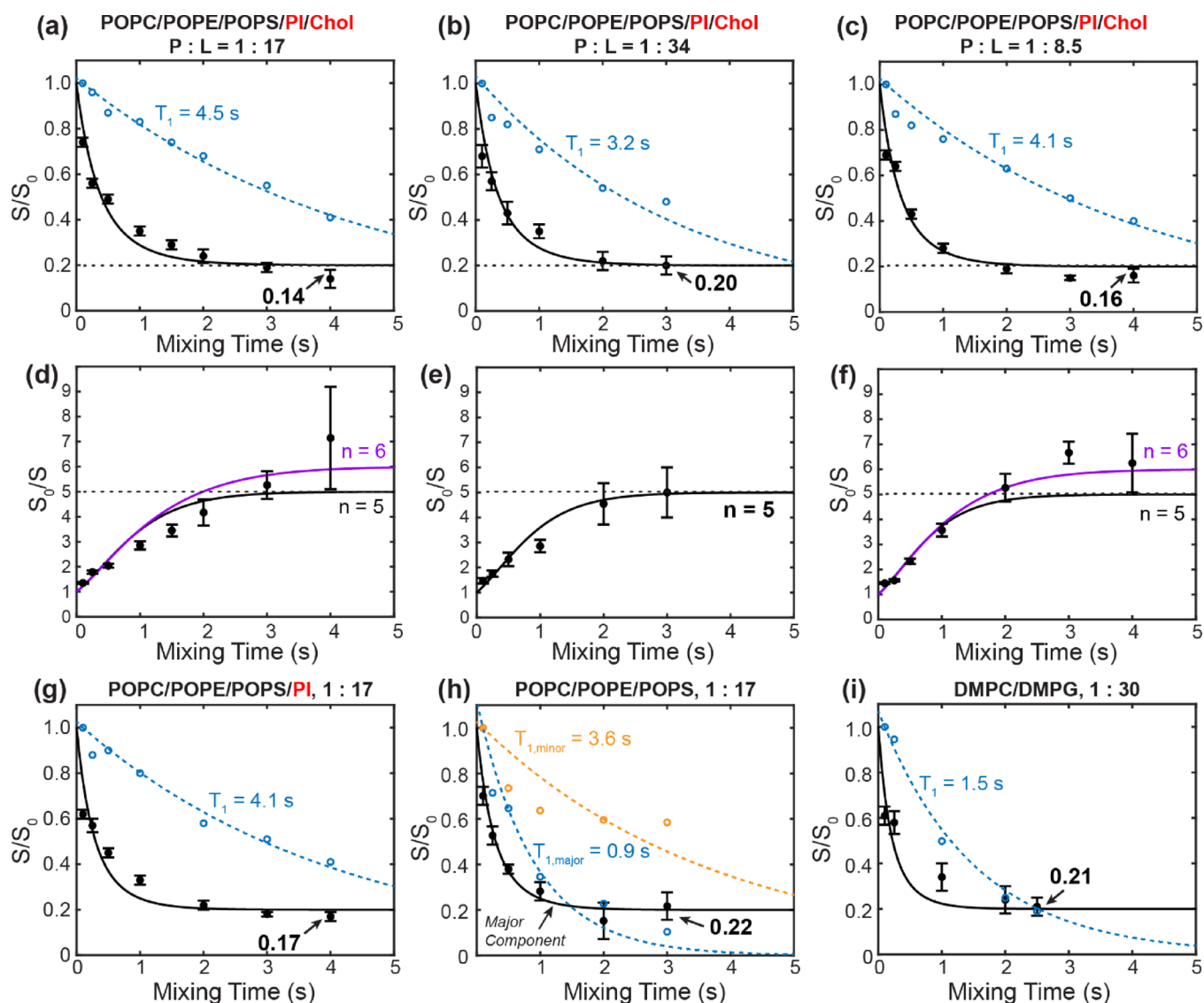
Figure 3. ^{19}F CODEX of 4-^{19}F-Phe23-labeled ETM in different lipid membranes at various peptide to phospholipid ratios (P:L). Filled circles are the measured CODEX S/S_0 values, while open circles are the intensity decays of the control spectra S_0, normalized to the 100 ms spectral intensity. Solid lines are the best-fit matrix simulations of the CODEX decay using an isolated symmetric oligomer model. Dashed lines are the best exponential fit to the S_0 decay to give the ^{19}F T_1 relaxation time. (a−c) CODEX decays of the ERGIC-bound ETM at varying P:L ratios. (a) P:L = 1:17. (b) P:L = 1:34. (c) P:L = 1:8.5. The best-fit curves use a symmetric pentamer model. (d−f) CODEX intensities shown as inverse S_0/S ratios for the same three samples as in (a−c), to better compare the pentamer and hexamer fits to the measured data at long mixing times. The best-fit simulations for a symmetric pentamer model (black) and a symmetric hexamer model (purple) are shown in (d) and (f). (g) CODEX decay of the ETM bound to a cholesterol-depleted ERGIC membrane (POPC/POPE/PI/POPS) at P:L = 1:17. (h) CODEX decay of the major Phe23 peak in POPC/POPE/POPS membrane-bound ETM at a P:L of 1:17. The S_0 decays of the major peak (blue open circles) and minor peak (orange open circles) indicate distinct T_1 relaxation times. (i) CODEX decay of the DMPC/DMPG-bound ETM at a P:L ratio of 1:30. The ^{19}F T_1 times are longer than 3 s in all membranes except for the major peak of the POPC/POPE/POPS-bound sample and the DMPC/DMPG-bound ETM.

and 3c). For example, at 2 and 3 s mixing, the 1:8.5 sample exhibits echo intensities of 0.19 ± 0.02 and 0.15 ± 0.01, respectively, which are significantly lower than the intensities of 0.24 ± 0.03 and 0.19 ± 0.02 for the 1:17 sample at these times (Table 2). These results confirm that as the peptide concentration increases, interpentamer ^{19}F−^{19}F dipolar couplings increasingly suppress the CODEX intensities at long mixing times. This conclusion is consistent with the restored long ^{19}F T_1 of 4.1 s for the highly concentrated 1:8.5 sample, again indicating that high peptide concentrations immobilize the peptide by clustering of the pentamers.

A plot of the inverse CODEX intensity ratios, S_0/S, more clearly differentiates the long-time behavior of the CODEX

data and clarifies the concentration-dependent supramolecular organization of the ETM in the ERGIC membrane (Figure 3d−f). The intensities of the 1:17 sample fit similarly well to n = 5 or n = 6, but neither matrix calculation fully reproduces both the short and long-time intensities of the data. This is indicative of the presence of two dipolar networks, those within a pentamer and between multiple pentamers (Figure 3d). In comparison, the inverse intensity ratios of the most diluted sample, at P:L = 1:34, clearly fit with n = 5 (Figure 3e). At the highest peptide concentration (1:8.5), the data better fit with a hexamer (n = 6) than a pentamer (n = 5), which can be attributed to significant interpentamer clustering (vide infra).

Table 2. Measured ^{19}F CODEX S/S_0 Values of 4-^{19}F-Phe23-Labeled ETM in All Lipid Membranes Examined in This Study^a

mixing time (s)	ERGIC P:L = 1:17	ERGIC P:L = 1:34	ERGIC P:L = 1:8.5	POPC/E/I/S P:L = 1:17	POPC/E/S P:L = 1:17	DMPC/G P:L = 1:30
0.10	0.74 ± 0.02	0.68 ± 0.05	0.69 ± 0.02	0.62 ± 0.02	0.70 ± 0.04	0.61 ± 0.04
0.25	0.56 ± 0.02	0.57 ± 0.04	0.64 ± 0.02	0.57 ± 0.03	0.53 ± 0.04	0.58 ± 0.05
0.50	0.49 ± 0.02	0.43 ± 0.05	0.43 ± 0.02	0.45 ± 0.02	0.38 ± 0.02	
1.00	0.35 ± 0.02	0.35 ± 0.03	0.28 ± 0.02	0.33 ± 0.02	0.28 ± 0.04	0.34 ± 0.06
1.50	0.29 ± 0.02					
2.00	0.24 ± 0.03	0.22 ± 0.04	0.19 ± 0.02	0.22 ± 0.02	0.15 ± 0.08	0.24 ± 0.06
2.50						0.21 ± 0.04
3.00	0.19 ± 0.02	0.20 ± 0.04	0.15 ± 0.01	0.18 ± 0.01	0.22 ± 0.06	
4.00	0.14 ± 0.03		0.16 ± 0.03	0.17 ± 0.02		
expt. time	66 h	106 h	50 h	132 h	72 h	181 h

^{a}Some phospholipids are indicated by their last letter for simplicity.

The CODEX results obtained from the 4-^{19}F-Phe23-labeled peptide are reproduced when fluorine labels are incorporated at two other positions. The 4-^{19}F-Phe20-labeled peptide showed a CODEX intensity of 0.31 ± 0.05 at 500 ms mixing (Figure 4a). This value is significantly lower than those
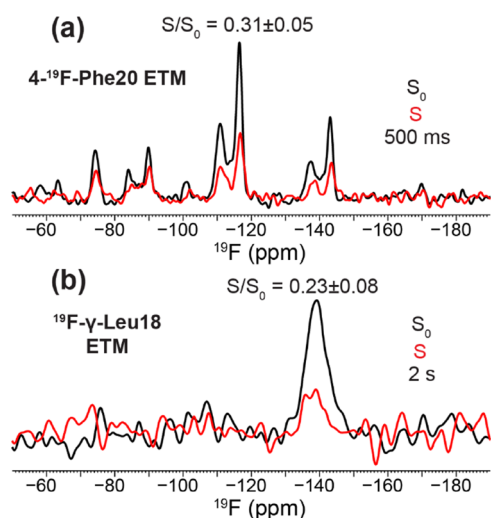
Figure 4. Additional ^{19}F NMR spectra of fluorinated ETM. (a) 500 ms CODEX control S_0 (black) and dephased S (red) spectra of 4-^{19}F-Phe20-labeled ETM bound to the ERGIC membrane at P:L = 1:13. The spectra were measured using a 400 MHz NMR spectrometer (9.4 T, ^{19}F Larmor frequency 376 MHz) under 10 kHz MAS at a thermocouple reported temperature of 248 K. (b) 2 s ^{19}F CODEX S_0 and S spectra of γ-^{19}F-Leu18-labeled ETM, bound to the ERGIC membrane at a P:L ratio of 1:17. The spectra were measured using a 600 MHz NMR spectrometer (14.1 Tesla, ^{19}F Larmor frequency 564 MHz) under 18 kHz MAS at a bearing temperature of 240 K.

measured on Phe23 samples at the same mixing time (Table 2) as spin diffusion is more rapid at 9.4 Tesla and 10 kHz MAS than at higher magnetic fields and faster MAS rates. The observed CODEX decay is consistent with a pentamer model while ruling out dimers and trimers. The two ^{19}F peaks for Phe20 have been recently shown to result from different sidechain conformations that correlate with channel closing and opening.[47] γ-^{19}F-Leu18-labeled ETM exhibited a CODEX S/S_0 intensity of 0.23 ± 0.08 at 2 s mixing (Figure 4b), consistent with a pentamer model.

To assess whether there is any motional contribution to the CODEX decay, we conducted additional control CODEX experiments at a higher temperature of 250 K. With 1 s mixing, the S/S_0 value is 0.36 ± 0.02 (data not shown), which is within the experimental uncertainty of the value at 240 K. With 2 s mixing, the S/S_0 value at 250 K is 0.20 ± 0.02, which is still within the uncertainty of the value at 240 K (Table 2). Thus, there is no detectable slow motion of the Phe23 sidechain to cause CODEX decay at the temperature, membrane composition, and peptide concentrations used in these experiments. Therefore, the CODEX intensities measured here exclusively reflect ^{19}F spin diffusion.

Supramolecular Organization of the ETM Is Affected by Phosphatidylinositol. The observed pentamer clustering, as shown by CODEX intensities below 0.20 at long mixing times, leads to the question of whether certain lipids in the ERGIC mixture are responsible for the clustering of multiple pentamers. To answer this question, we reconstituted 4-^{19}F-Phe23-labeled ETM into three simplified lipid membranes. We first tested a cholesterol-free ERGIC membrane, which contains only the four phospholipids (Table 1). This membrane was chosen based on the recent NMR evidence that cholesterol binds to and mediates the clustering of influenza M2,[48,49] HIV gp41,[50,51] and the amyloid precursor protein[52] in lipid membranes. Contrary to this hypothesis, the cholesterol-free ERGIC-bound ETM at P:L = 1:17 gives a similar CODEX equilibrium intensity of 0.17 ± 0.02 at 4 s (Figures 2e and 3g, Table 2). The cholesterol-free sample also displays a long ^{19}F T_1 relaxation time of 4.1 s. Thus, the presence or absence of cholesterol in the ERGIC membrane does not affect pentamer clustering.

We next simplified the membrane further by removing both phosphatidylinositol and cholesterol. Interestingly, this ternary mixture, POPC/POPS/POPE, produced substantial spectral changes. The minor component at −111 ppm increased its intensity relative to the major peak at −115 ppm in the CP spectrum compared to the other samples (Figure 2a), to about 25% of the total integrated intensity of the two peaks. Moreover, the downfield signal has a similarly long ^{19}F T_1 relaxation time (3.6 s) as in the ERGIC membranes, while the upfield peak has a much shorter T_1 of 0.9 s (Figure 3h). As a result of these dramatically different T_1 relaxation times, the two peaks have similar S_0 intensities (60% downfield: 40% upfield) at long CODEX mixing times (Figure 2f) in qualitative contrast to the other samples. Thus, in the absence of phosphatidylinositol, two populations of the ETM oligomers are present in the membrane, a minor component (∼25%) of immobilized peptide with long T_1 and a major component of more dynamic peptide. The distinct T_1 relaxation behaviors
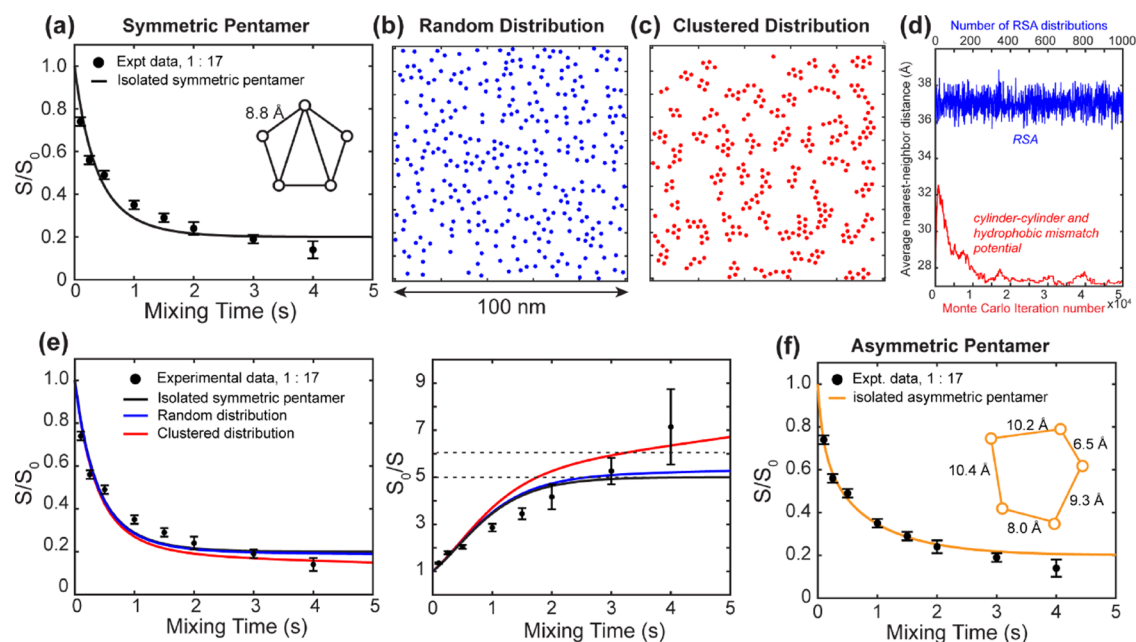
Figure 5. Alternative ETM oligomerization models and their corresponding CODEX simulations. The experimental data (filled circles) are those of ERGIC-bound 4-^{19}F-Phe23-labeled ETM at P:L = 1:17. Simulated CODEX decays are shown in solid lines. (a) Measured CODEX decays together with best-fit simulation using an isolated symmetric pentamer model. The simulation is the same as in Figure 3a. The nearest-neighbor distance of the best-fit pentamer is 8.8 Å. While the overall agreement between the experiment and simulation is good (χ^2_ν = 1.01), the intensities deviate at intermediate (1−2 s) and long mixing times (4 s). (b) Simulated RSA distribution of pentamers in a 100 × 100 nm^2 square. All couplings stronger than 0.85 Hz (50 Å) are considered in the calculation, though convergence occurs around 15 Å. (c) Simulated cluster distribution of pentamers based on a cylinder−cylinder interaction and hydrophobic mismatch model. (d) Measured CODEX decays shown as S/S_0 and the inverse S_0/S values. These are overlaid with simulated curves for the isolated symmetric pentamer model, the random distribution model, and the clustered distribution model. The clustered pentamer model agrees best with the measured CODEX intensities at long mixing times. (e) Average nearest-neighbor distances from the RSA simulation (blue) and the cluster simulation (red). The distances from the RSA distribution were obtained from 1000 independent simulations. The distances from the interaction potential simulation were obtained from 50,000 Monte Carlo steps to reach a final distribution. (f) Experimental CODEX data with best-fit simulation using an isolated asymmetric pentamer model. Gradient decent fitting yielded better agreement between the experiment and simulations compared to (a), and the nearest-neighbor distances in the model range from 6.5 to 10.4 Å.

could reflect the heterogeneous dynamics of the entire peptide or the Phe20 sidechain alone. These two populations are not in close contact, as no cross peaks are observed in 2D ^{19}F correlation spectra even after 400 ms of Combined R2$_n^\nu$-Driven (CORD) spin diffusion[53] (Figure S2). The CODEX intensities of the major component show similarly low S/S_0 values as the peptide in other membranes. At 3 s, the intensity is 0.22 ± 0.06, indicating that the ETM remains pentameric in this ternary membrane.

Finally, we bound 4-^{19}F-Phe23 labeled-ETM to the model membrane DMPC/DMPG at a P:L of 1:30. In the absence of cholesterol and phosphatidylinositol and at this relatively low peptide concentration, this membrane sample provides a control for the propensity of the ETM to self-assemble in lipid bilayers. We measured a CODEX intensity of 0.21 ± 0.04 at 2.5 s (Figures 2g and 3i), again indicating a pentamer. The ^{19}F T_1 of the peptide is 1.5 s, suggesting that the ETM pentamers are not clustered under this condition.

To gain insight into the possible arrangements of the ETM pentamers in the clusters and whether they agree with the measured CODEX intensities at long mixing times, we simulated a random distribution and clustered distribution of oligomers. For isolated symmetric pentamers, the CODEX simulation yielded a best-fit pentamer side length of 8.8 Å (Figure 5a). As shown above, this does not fully reproduce the experimental data at long mixing times. To generate a random distribution of pentamers without interoligomer interactions,

we implemented the RSA method, whose resulting distribution in a 100 × 100 nm^2 square is shown in Figure 5b. This RSA distribution produces interoligomer distances that are, on average, approximately half of those in a regular lattice model. A 100 × 100 nm^2 square should be occupied by approximately 325 oligomers (eq 1). In a regular lattice, the interoligomer spacing is approximately 55 Å. With RSA, the average nearest-neighbor distance from the center of one oligomer to the next decreases to 37 Å. Subtracting twice the channel radius (13 Å) gives an approximate average ^{19}F−^{19}F distance of 11 Å, which is within the detectable range by ^{19}F spin diffusion NMR.[54] However, since the rate of ^{1}H-driven spin diffusion depends on r^{-6}, a 11 Å distance on average is only a small correction to the intraoligomer distance of ~9 Å in the isolated pentamer model. To reproduce the experimentally measured CODEX dephasing, a more specific clustering model is required. We adopted a potential of mean force that accounts for both protein shape and protein−lipid hydrophobic mismatch (Figure S3)[39] and simulated the resulting distribution using a Metropolis Monte Carlo method (Figure 5c). The calculated CODEX S/S_0 and S_0/S curves for these two models are compared with the isolated pentamer simulation in Figure 5d. The RSA distribution produced only a minor intensity reduction at long mixing times and thus does not significantly improve the fit over the isolated pentamer fit. The cluster distribution resulted in a noticeable decrease in S/S_0 intensity at long mixing times and agreed much better with the experimental
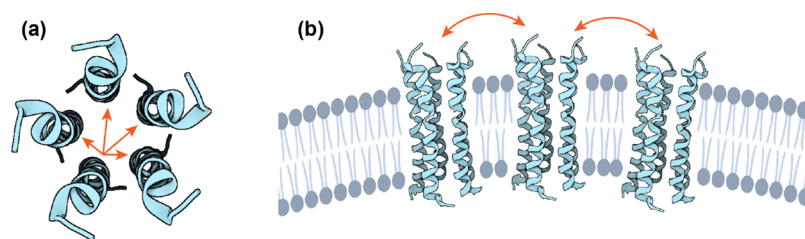
Figure 6. SARS-CoV-2 ETM forms pentameric α-helical bundles in lipid bilayers. (a) Top view of the ETM pentamer structure, using the solid-state NMR structural model of the closed state of the ETM (PDB: 7K3G).[8] Intrapentamer ^{19}F spin diffusion is indicated by arrows. (b) Model of the clustering of ETM pentamers in ERGIC-mimetic phosphatidylinositol containing lipid bilayers at high peptide concentrations. Spin diffusion between different pentamers is illustrated by arrows.

CODEX intensities. Therefore, interpentamer contacts, which are only significant in the clustered distribution (Figure 5e), reproduce the observed intensity decays below 0.20 at long mixing times. The improved fit at long mixing times still does not fully reproduce the measured intensities at intermediate mixing times between 1 and 2 s. Instead, these intensities are well-described by asymmetric pentamers (Figure 5f). This suggests that the 4-^{19}F label at the Phe23 sidechains may exhibit some rotameric disorder, leading to inequivalent distances between adjacent subunits, as represented by an asymmetric pentamer.

Calibration of the Overlap Integral F(0). The overlap integral $F_{ij}(0)$ is the probability that single-quantum transitions occur at the same frequency for spin i and spin j. It is related to the normalized zero-quantum line shape at zero frequency. As in the existing literature,[43,44,54−57] here we treat $F(0)$ as a parameter to be calibrated from known crystal structures. ^{19}F CODEX of 5-^{19}F-trptophan (Figure S4a) shows an exponential decay to $S/S_0 = 0.50$ at 400 ms. Fitting to $0.5 + 0.5e^{-ct}$ shows excellent agreement with the experimental data ($R^2 = 0.9935$) for the time constant $c = 183$ s^{-1} (Figure S4b). Using the known crystal structure of L-tryptophan hydrochloride,[58] we calibrated the $F(0)$ value. L-Tryptophan hydrochloride crystallized in the $P2_1$ space group, with two orientationally inequivalent molecules in the unit cell. The nearest neighbor H5−H5 distance in the lattice is 4.62 Å. Second moment analysis, summing over additional unit cells until the effective dipolar coupling converges, gives an effective ^{19}F−^{19}F dipolar coupling of 4.99 kHz, which corresponds to an effective distance of 4.16 Å. The rate of ^{1}H-driven spin diffusion driving CODEX is given by $k_{ij} = 0.5 \pi \omega_{ij} F_{ij}(0)$.[19,59] The dipolar coupling (ω_{ij}) is given by the dipolar coupling constant, $(\mu_0 \hbar \gamma^2)/(4\pi r^3)$ and the powder averaged angular dependence, $\langle ((1 - 3\cos^2\theta_{ij})/2)^2 \rangle = 0.2$. Calculating the dipolar coupling based on the converged effective ^{19}F−^{19}F distance allowed the extraction of an $F(0)$ value of 3.4 ± 0.4 μs. A detailed description of the calculation of $F(0)$ is given in the Supporting Information. Performing CODEX matrix calculations at varying $F(0)$ values yields identical results as the exponential fitting does (Figure S4c,d).

This $F(0)$ value is an order of magnitude smaller than the previously reported value of 37 μs by our group.[19] The previous value was measured under 8 kHz MAS on a 9.4 T magnet and should be comparable to the measurements in this work. Recalculation based on the previous data indicates that the previously reported $F(0)$ value incorporated an additional factor of π^2, which was also applied in the matrix calculation scripts for the CODEX simulations. The $F(0)$ values were first obtained from the CODEX decay of samples with known

crystal structures, and then, these $F(0)$ values were used in CODEX calculations with unknown distances. Since the same equation with an error of π^2 was used both to calibrate and to determine unknown distances, the previously reported distances are correct, and only the numerical value of $F(0)$ was mis-reported. Correcting for this π^2 factor, the true $F(0)$ value should be 3.7 μs for ^{19}F and 8.0 μs for ^{13}C. Other literature values for $F(0)$ of ^{13}C spins range from 1.2 to 11.4 μs,[55,57] in agreement with the revised value.

■ DISCUSSION

SARS-CoV-2 ETM Forms Pentameric Channels That Cluster in Lipid Membranes. The CODEX data obtained here for six ETM samples show that the basic unit of assembly of the ETM in lipid bilayers is a pentamer (Figure 6a). In four membrane mixtures and at three peptide concentrations, the CODEX intensities of 4-^{19}F Phe23 decay to a value between 0.15 and 0.22 at 3 s. At the lowest peptide concentration where interoligomer contact is minimal, the CODEX intensities equilibrate to 0.20 (Figure 3b,e). Thus, when the protein is sufficiently dilute in the membrane so that ^{19}F spin diffusion is restricted to isolated channels, the stoichiometry of the complex can be established to be a pentamer. At higher peptide concentrations, the CODEX intensities decrease below 0.20 in ERGIC-mimetic and phosphatidylinositol-containing membranes, indicating that the pentamers cluster under these conditions (Figure 6b).

The low CODEX intensities of less than 0.25 at mixing times longer than 2 s (Table 2) rule out a substantial population of small oligomers such as dimers and trimers. If we assume 20% to be the lower limit of the population of oligomeric species that can be detected by NMR, then a mixture of 20% dimers and 80% pentamers would give a CODEX equilibrium value of 0.26. This is significantly higher than the measured CODEX equilibrium values of 0.20 for the three ERGIC samples (Table 2). Alternatively, if a dimer is assumed to coexist with a hexamer, then the dimer fraction cannot be larger than 10% in order to agree with the data. Thus, the experimental data rule out the presence of a sizeable fraction of small oligomers.

Furthermore, the ^{13}C, ^{15}N, and ^{19}F spectral linewidths of membrane-bound ETM rule out the coexistence of two distinctly different subunit stoichiometries. We found narrow ^{13}C linewidths of ~0.5 ppm and ^{15}N linewidths of ~0.9 ppm for the protein, implying a highly homogeneous protein conformation for both the backbone and sidechain. The ^{19}F linewidths of 4-^{19}F Phe23 are ~1.5 ppm, implying that the helix−helix interface of the ETM oligomer is also structurally homogeneous. This high degree of homogeneity coupled with

a lack of peak doubling makes the presence of two distinct structural states, a dimer and hexamer, or a pentamer and heptamer for example, highly unlikely.

Is it possible that the ETM forms a mixture of similarly high-molecular-weight oligomers such as tetramers and hexamers or pentamers and heptamers? Such a mixture cannot be ruled out based on the CODEX data alone. However, we consider this scenario unlikely because even a modest change of the oligomer number will affect the sidechain packing between neighboring helices, which should cause broad ^{19}F peaks. The ^{19}F spectra of 4-^{19}F-Phe23 exhibit a dominant peak at −115 ppm that accounts for 75−95% of the spectral intensity and a minor peak at −111 ppm that represents 5−25% of the spectral intensities. The minor peak became more discernible in the POPC/POPE/POPS membrane due to its long ^{19}F T_1 relaxation time compared to the T_1 of the major peak (Figures 2f and 3h). However, its CODEX intensities are not different from those of the major component within experimental uncertainty. Therefore, for all the lipid membranes examined here, we do not find evidence for a coexistence of multiple oligomeric states.

The stoichiometry of virus membrane proteins can vary in different membrane-mimetic environments. The influenza viroporin, M2, is stably tetrameric in detergents and lipid bilayers, as shown by AUC experiments in detergent micelles,[17,18] solid-state NMR CODEX data in lipid bilayers,[19,20] and X-ray crystal structures in lipid cubic phases.[22] Moreover, whole cell current measurements in oocytes that express a mixture of amantadine-sensitive wild-type M2 and amantadine-resistant mutant M2 definitively showed that the tetrameric state is the functionally active state.[16] The HIV viroporin Vpu forms pentamers based on gel filtration chromatography data,[25] and the pentamer is suggested to be the most thermodynamically stable species by molecular dynamics simulations.[24] However, evidence for stoichiometries from tetramers to hexamers has also been reported from crosslinking, gel electrophoresis, and AUC data in lipid bilayers.[26,60] The dual-TM-helix hepatitis c virus p7 protein (HCV p7) can adopt either hexamers or heptamers depending on the membrane-mimetic environments.[61−64] Compared to these viroporins, SARS-CoV-2 ETM forms stable pentamers in lipid bilayers based on the data shown here. The observation of multiple oligomeric states in various detergents might reflect different structures of the protein formed in these non-native environments and the small differences in thermodynamic stabilities between different oligomeric assemblies.

Increasing experimental evidence has shown that membrane proteins often cluster for function. Ion channels such as KcsA[65] and mammalian K$^+$ and Ca^{2+} channels[66,67] have been reported to cluster in the membrane to cause coupled gating. Influenza M2[68,69] and HIV-1 gp41[50] have been recently shown to cluster in the membrane, mediated by cholesterol.[48,49,51] This clustering is implicated in membrane curvature generation and may be used by both proteins to achieve their membrane scission and membrane fusion functions, respectively. Electron microscopy studies of the mouse hepatitis virus suggest that its E protein induces membrane curvature.[70] SARS-CoV-2 E has a similar role in viral particle formation,[71] and thus, its clustering might help to generate membrane curvature. Fluorescence microscopy data of the subcellular localization of the three membrane proteins (S, M, and E) of the SARS-CoV-1 virus found that the E protein forms large membrane clusters that

co-localize with endoplasmic reticulum markers,[2,72] but molecular evidence of clustering of E had not been reported until now. The current finding that the ETM clusters in the ERGIC-mimetic lipid membrane explains the high rigidity of the peptide in this membrane at ambient temperature.[8] Unlike M2 and gp41, clustering of the SARS-CoV-2 E pentamers in lipid membranes is not induced by cholesterol alone. Removal of cholesterol did not raise the CODEX intensities at long mixing times or decrease the ^{19}F T_1 (Figure 3g). Instead, removing both cholesterol and phosphatidylinositol is required to increase the CODEX intensity to about 0.20 (Figure 3h), which is diagnostic of dispersal of clusters. The isolation of the E pentamers is also manifested by the significantly shortened ^{19}F T_1 relaxation time. This result is reproduced in the model membrane DMPC/DMPG, in which the ETM exhibits isolated pentamers with a short ^{19}F T_1. Thus, supramolecular assembly of ETM pentamers requires the presence of phosphatidylinositol.

The surprising finding that phosphatidylinositol is required for ETM clustering is intriguing. Phosphatidylinositol and its phosphorylated derivatives such as phosphatidylinositol 4,5-bisphosphate (PIP$_2$) and phosphatidylinositol 3,4,5-triphosphate (PIP$_3$) are known to self-associate in the membrane in the presence of divalent cations such as calcium[73] and can induce clustering of membrane proteins such as syntaxin-1A to mediate membrane fusion in neurons.[74−76] Conversely, some membrane proteins have been reported to associate with and induce clustering of phosphatidylinositol to carry out functions such as signal transduction.[77] Moreover, calcium ions are known to cluster anionic phosphatidylserine and phosphatidylinositol.[78,79] Thus, the current finding that the calcium-conducting E channel is clustered by phosphatidylinositol suggests that calcium ions, which are present at much higher concentrations inside the ERGIC than in the cytoplasm, may have the dual action of clustering the E protein via phosphatidylinositol as well as permeating these clustered channels. Future studies should investigate how phosphatidylinositol binds E in the supramolecular assembly in the membrane and whether and how this interaction facilitates virus assembly and budding.

Structural Implications of the Interhelical Distances between Phe23 Sidechains. Simulation of the ^{19}F CODEX decay curves yielded nearest-neighbor intrapentamer distances of 8−9 Å for the 4-^{19}F-Phe23 labels. This distance is relatively independent of the membrane composition. Previous work by our group solved a 2.1-Å structure of the ETM at neutral pH.[8] In this structure, Phe23 occupies the heptad position *f*, interacting with lipids. This configuration would give a nearest-neighbor distance of ~15 Å, which is much longer than observed by the current CODEX data. The interhelical ^{13}C−^{19}F distance constraints that contributed to the structure calculation were measured using recombinant triply fluorinated ETM samples at the three Phe residues. Thus, the sidechain conformations in this closed-state ETM structural model will need to be revised using more extensive distance measurements to accommodate the shorter Phe23−Phe23 distances seen in the CODEX data here. Already, the current ^{19}F spectra of Phe23 indicate that this residue has a single predominant sidechain conformation, which differs from the dual-conformations seen for Phe20 and Phe26, which each manifest two ^{19}F peaks.[47] We recently showed that these two sidechain rotamers of Phe20 and Phe26 correspond to a lipid-facing conformer and a more water-accessible conformer at the

helix−helix interface. In comparison, the distinct ^{19}F spectra of Phe23 indicate that Phe23 adopts a single rotamer that may point either to the pore or to the helix−helix interface to occlude the channel at neutral pH. In the influenza M2 transmembrane peptide, aromatic gating is accomplished by a pore-facing Trp residue.[44,80−84] The HCV p7 channel also contains three Phe residues at positions 22, 25, and 26. Joint mutations of these three residues to Ala increased the channel activity, suggesting that aromatic interactions within this Phe stack restrict ion current.[85] Thus, the HCV p7 channel bears interesting similarities to the SARS-CoV-2 E channel. Future studies to probe how these Phe residues stabilize the five-helix bundle and regulate channel gating will be important for elucidating the structure−function relation of the E protein.

■ ASSOCIATED CONTENT

Ⓢ Supporting Information

The Supporting Information is available free of charge at https://pubs.acs.org/doi/10.1021/acs.biochem.2c00464.

> Additional details about the calculation of the overlap integral $F(0)$, MALDI-MS data of ETM peptides, additional NMR spectra, plots of average nearest-neighbor distances from the RSA and Monte Carlo simulations, 5-^{19}F-Trp $F(0)$ calibration data, pairwise interaction potential used, and MATLAB code for simulating CODEX, RSA, and pore clustering (PDF)

Accession Codes

The full-length SARS-CoV-2 E protein sequence can be found at NCBI YP_009724392.1, (residues 1−75).

■ AUTHOR INFORMATION

Corresponding Author

   Mei Hong − *Department of Chemistry, Massachusetts Institute of Technology, Cambridge, Massachusetts 02139, United States;* ⓞ orcid.org/0000-0001-5255-5858; Email: meihong@mit.edu

Authors

   Noah H. Somberg − *Department of Chemistry, Massachusetts Institute of Technology, Cambridge, Massachusetts 02139, United States*

   Westley W. Wu − *Department of Chemistry, Massachusetts Institute of Technology, Cambridge, Massachusetts 02139, United States*

   João Medeiros-Silva − *Department of Chemistry, Massachusetts Institute of Technology, Cambridge, Massachusetts 02139, United States;* ⓞ orcid.org/0000-0003-3532-4390

   Aurelio J. Dregni − *Department of Chemistry, Massachusetts Institute of Technology, Cambridge, Massachusetts 02139, United States;* ⓞ orcid.org/0000-0003-3422-4734

   Hyunil Jo − *Department of Pharmaceutical Chemistry, University of California, San Francisco, San Francisco, California 94158, United States;* ⓞ orcid.org/0000-0002-4863-0779

   William F. DeGrado − *Department of Pharmaceutical Chemistry, University of California, San Francisco, San Francisco, California 94158, United States*

Complete contact information is available at:
https://pubs.acs.org/10.1021/acs.biochem.2c00464

Notes

The authors declare no competing financial interest.

■ REFERENCES

(1) Weiss, S. R.; Navas-Martin, S. Coronavirus pathogenesis and the emerging pathogen severe acute respiratory syndrome coronavirus. *Microbiol. Mol. Biol. Rev.* **2005**, *69*, 635−664.

(2) Schoeman, D.; Fielding, B. C. Coronavirus envelope protein: current knowledge. *Virol. J.* **2019**, *16*, 69.

(3) Nieva, J. L.; Madan, V.; Carrasco, L. Viroporins: structure and biological functions. *Nat. Rev. Microbiol.* **2012**, *10*, 563−574.

(4) Nieto-Torres, J. L.; DeDiego, M. L.; Verdia-Baguena, C.; Jimenez-Guardeno, J. M.; Regla-Nava, J. A.; Fernandez-Delgado, R.; Castano-Rodriguez, C.; Alcaraz, A.; Torres, J.; Aguilella, V. M.; Enjuanes, L. Severe acute respiratory syndrome coronavirus envelope protein ion channel activity promotes virus fitness and pathogenesis. *PLoS Pathog.* **2014**, *10*, No. e1004077.

(5) Xia, B.; Shen, X.; He, Y.; Pan, X.; Liu, F. L.; Wang, Y.; Yang, F.; Fang, S.; Wu, Y.; Duan, Z.; Zuo, X.; Xie, Z.; Jiang, X.; Xu, L.; Chi, H.; Li, S.; Meng, Q.; Zhou, H.; Zhou, Y.; Cheng, X.; Xin, X.; Jin, L.; Zhang, H. L.; Yu, D. D.; Li, M. H.; Feng, X. L.; Chen, J.; Jiang, H.; Xiao, G.; Zheng, Y. T.; Zhang, L. K.; Shen, J.; Li, J.; Gao, Z. SARS-CoV-2 envelope protein causes acute respiratory distress syndrome (ARDS)-like pathological damages and constitutes an antiviral target. *Cell Res.* **2021**, *31*, 847−860.

(6) Zumla, A.; Chan, J. F.; Azhar, E. I.; Hui, D. S.; Yuen, K. Y. Coronaviruses - drug discovery and therapeutic options. *Nat. Rev. Drug. Discov.* **2016**, *15*, 327−347.

(7) Śledź, P.; Caflisch, A. Protein structure-based drug design: from docking to molecular dynamics. *Curr. Opin. Struct. Biol.* **2018**, *48*, 93−102.

(8) Mandala, V. S.; McKay, M. J.; Shcherbakov, A. A.; Dregni, A. J.; Kolocouris, A.; Hong, M. Structure and drug binding of the SARS-CoV-2 envelope protein transmembrane domain in lipid bilayers. *Nat. Struct. Mol. Biol.* **2020**, *27*, 1202−1208.

(9) Li, Y.; Surya, W.; Claudine, S.; Torres, J. Structure of a conserved Golgi complex-targeting signal in coronavirus envelope proteins. *J. Biol. Chem.* **2014**, *289*, 12535−12549.

(10) Parthasarathy, K.; Ng, L.; Lin, X.; Liu, D. X.; Pervushin, K.; Gong, X.; Torres, J. Structural flexibility of the pentameric SARS coronavirus envelope protein ion channel. *Biophys. J.* **2008**, *95*, L39−L41.

(11) Parthasarathy, K.; Lu, H.; Surya, W.; Vararattanavech, A.; Pervushin, K.; Torres, J. Expression and purification of coronavirus envelope proteins using a modified β-barrel construct. *Protein Expression Purif.* **2012**, *85*, 133−141.

(12) Torres, J.; Wang, J.; Parthasarathy, K.; Liu, D. X. The Transmembrane Oligomers of Coronavirus Protein E. *Biophys. J.* **2005**, *88*, 1283−1290.

(13) Surya, W.; Li, Y.; Verdià-Bàguena, C.; Aguilella, V. M.; Torres, J. MERS coronavirus envelope protein has a single transmembrane domain that forms pentameric ion channels. *Virus Res.* **2015**, *201*, 61−66.

(14) Westerbeck, J. W.; Machamer, C. E. A Coronavirus E Protein Is Present in Two Distinct Pools with Different Effects on Assembly and the Secretory Pathway. *J. Virol.* **2015**, *89*, 9313–9323.

(15) Ruch, T. R.; Machamer, C. E. A Single Polar Residue and Distinct Membrane Topologies Impact the Function of the Infectious Bronchitis Coronavirus E Protein. *PLoS Pathog.* **2012**, *8*, No. e1002674.

(16) Sakaguchi, T.; Tu, Q.; Pinto, L. H.; Lamb, R. A. The active oligomeric state of the minimalistic influenza virus M_2 ion channel is a tetramer. *Proc. Natl. Acad. Sci. U. S. A.* **1997**, *94*, 5000–5005.

(17) Salom, D.; Hill, B. R.; Lear, J. D.; DeGrado, W. F. pH-dependent tetramerization and amantadine binding of the transmembrane helix of M2 from the influenza A virus. *Biochemistry* **2000**, *39*, 14160–14170.

(18) Howard, K. P.; Lear, J. D.; DeGrado, W. F. Sequence determinants of the energetics of folding of a transmembrane four-helix-bundle protein. *Proc. Natl. Acad. Sci. U. S. A.* **2002**, *99*, 8568–8572.

(19) Luo, W.; Hong, M. Determination of the Oligomeric Number and Intermolecular Distances of Membrane Protein Assemblies by Anisotropic ^{1}H-Driven Spin Diffusion NMR Spectroscopy. *J. Am. Chem. Soc.* **2006**, *128*, 7242–7251.

(20) Williams, J. K.; Zhang, Y.; Schmidt-Rohr, K.; Hong, M. pH-Dependent Conformation, Dynamics, and Aromatic Interaction of the Gating Tryptophan Residue of the Influenza M2 Proton Channel from Solid-State NMR. *Biophys. J.* **2013**, *104*, 1698–1708.

(21) Stouffer, A. L.; Acharya, R.; Salom, D.; Levine, A. S.; Di Costanzo, L.; Soto, C. S.; Tereshko, V.; Nanda, V.; Stayrook, S.; DeGrado, W. F. Structural basis for the function and inhibition of an influenza virus proton channel. *Nature* **2008**, *451*, 596–599.

(22) Thomaston, J. L.; Woldeyes, R. A.; Nakane, T.; Yamashita, A.; Tanaka, T.; Koiwai, K.; Brewster, A. S.; Barad, B. A.; Chen, Y.; Lemmin, T.; Uervirojnangkoorn, M.; Arima, T.; Kobayashi, J.; Masuda, T.; Suzuki, M.; Sugahara, M.; Sauter, N. K.; Tanaka, R.; Nureki, O.; Tono, K.; Joti, Y.; Nango, E.; Iwata, S.; Yumoto, F.; Fraser, J. S.; DeGrado, W. F. XFEL structures of the influenza M2 proton channel: Room temperature water networks and insights into proton conduction. *Proc. Natl. Acad. Sci. U. S. A.* **2017**, *114*, 13357–13362.

(23) González, M. E. Vpu Protein: The Viroporin Encoded by HIV-1. *Viruses* **2015**, *7*, 4352–4368.

(24) Padhi, S.; Khan, N.; Jameel, S.; Priyakumar, U. D. Molecular dynamics simulations reveal the HIV-1 Vpu transmembrane protein to form stable pentamers. *PLoS One* **2013**, *8*, No. e79779.

(25) Hussain, A.; Das, S. R.; Tanwar, C.; Jameel, S. Oligomerization of the human immunodeficiency virus type 1 (HIV-1) Vpu protein–a genetic, biochemical and biophysical analysis. *Virol. J.* **2007**, *4*, 81.

(26) Sharpe, S.; Yau, W. M.; Tycko, R. Structure and dynamics of the HIV-1 Vpu transmembrane domain revealed by solid-state NMR with magic-angle spinning. *Biochemistry* **2006**, *45*, 918–933.

(27) Buffy, J. J.; Waring, A. J.; Hong, M. Determination of Peptide Oligomerization in Lipid Membranes with Magic-Angle Spinning Spin Diffusion NMR. *J. Am. Chem. Soc.* **2005**, *127*, 4477–4483.

(28) deAzevedo, E. R.; Bonagamba, T. J.; Hu, W.; Schmidt-Rohr, K. Centerband-only detection of exchange: efficient analysis of dynamics in solids by NMR. *J. Am. Chem. Soc.* **1999**, *121*, 8411–8412.

(29) deAzevedo, E. R.; Bonagamba, T. J.; Hu, W.; Schmidt-Rohr, K. Principle of centerband-only detection of the exchange and extension to a four-time CODEX. *J. Chem. Phys.* **2000**, *112*, 8988–9001.

(30) Hong, M.; Schmidt-Rohr, K. Magic-angle-spinning NMR techniques for measuring long-range distances in biological macro-molecules. *Acc. Chem. Res.* **2013**, *46*, 2154–2163.

(31) Simon, M. D.; Heider, P. L.; Adamo, A.; Vinogradov, A. A.; Mong, S. K.; Li, X.; Berger, T.; Policarpo, R. L.; Zhang, C.; Zou, Y.; Liao, X.; Spokoyny, A. M.; Jensen, K. F.; Pentelute, B. L. Rapid flow-based peptide synthesis. *ChemBioChem* **2014**, *15*, 713–720.

(32) Paquet, A. Introduction of 9-fluorenylmethyloxycarbonyl, trichloroethoxycarbonyl, and benzyloxycarbonyl amine protecting

(33) Schweizer, A.; Clausen, H.; van Meer, G.; Hauri, H. P. Localization of O-glycan initiation, sphingomyelin synthesis, and glucosylceramide synthesis in Vero cells with respect to the endoplasmic reticulum-Golgi intermediate compartment. *J. Biol. Chem.* **1994**, *269*, 4035–4041.

(34) Casares, D.; Escribá, P. V.; Rosselló, C. A. Membrane Lipid Composition: Effect on Membrane and Organelle Structure, Function and Compartmentalization and Therapeutic Avenues. *Int. J. Mol. Sci.* **2019**, *20*, 2167.

(35) van Meer, G.; Voelker, D. R.; Feigenson, G. W. Membrane lipids: where they are and how they behave. *Nat. Rev. Mol. Cell Biol.* **2008**, *9*, 112–124.

(36) Hills, R. D., Jr.; McGlinchey, N. Model parameters for simulation of physiological lipids. *J. Comput. Chem.* **2016**, *37*, 1112–1118.

(37) Leftin, A.; Molugu, T. R.; Job, C.; Beyer, K.; Brown, M. F. Area per lipid and cholesterol interactions in membranes from separated local-field ^{13}C NMR spectroscopy. *Biophys. J.* **2014**, *107*, 2274–2286.

(38) Evans, J. W. Random and cooperative sequential adsorption. *Rev. Mod. Phys.* **1993**, *65*, 1281–1329.

(39) Morozova, D.; Weiss, M.; Guigas, G. Shape as a determinant of membrane protein cluster formation. *Soft Matter* **2012**, *8*, 11905–11910.

(40) Metropolis, N.; Rosenbluth, A. W.; Rosenbluth, M. N.; Teller, A. H.; Teller, E. Equation of State Calculations by Fast Computing Machines. *J. Chem. Phys.* **1953**, *21*, 1087–1092.

(41) Verdiá-Báguena, C.; Nieto-Torres, J. L.; Alcaraz, A.; DeDiego, M. L.; Torres, J.; Aguilella, V. M.; Enjuanes, L. Coronavirus E protein forms ion channels with functionally and structurally-involved membrane lipids. *Virology* **2012**, *432*, 485–494.

(42) Nieto-Torres, J. L.; Dediego, M. L.; Alvarez, E.; Jiménez-Guardeño, J. M.; Regla-Nava, J. A.; Llorente, M.; Kremer, L.; Shuo, S.; Enjuanes, L. Subcellular location and topology of severe acute respiratory syndrome coronavirus envelope protein. *Virology* **2011**, *415*, 69–82.

(43) Kwon, B.; Lee, M.; Waring, A. J.; Hong, M. Oligomeric Structure and Three-Dimensional Fold of the HIV gp41 Membrane-Proximal External Region and Transmembrane Domain in Phospholipid Bilayers. *J. Am. Chem. Soc.* **2018**, *140*, 8246–8259.

(44) Kwon, B.; Roos, M.; Mandala, V. S.; Shcherbakov, A. A.; Hong, M. Elucidating Relayed Proton Transfer through a His-Trp-His Triad of a Transmembrane Proton Channel by Solid-State NMR. *J. Mol. Biol.* **2019**, *431*, 2554–2566.

(45) Lee, M.; Yao, H.; Kwon, B.; Waring, A. J.; Ruchala, P.; Singh, C.; Hong, M. Conformation and Trimer Association of the Transmembrane Domain of the Parainfluenza Virus Fusion Protein in Lipid Bilayers from Solid-State NMR: Insights into the Sequence Determinants of Trimer Structure and Fusion Activity. *J. Mol. Biol.* **2018**, *430*, 695–709.

(46) Salnikov, E. S.; Raya, J.; De Zotti, M.; Zaitseva, E.; Peggion, C.; Ballano, G.; Toniolo, C.; Raap, J.; Bechinger, B. Alamethicin Supramolecular Organization in Lipid Membranes from (19)F Solid-State NMR. *Biophys. J.* **2016**, *111*, 2450–2459.

(47) Medeiros-Silva, J.; Somberg, N. H.; Wang, H. K.; McKay, M. J.; Mandala, V. S.; Dregni, A. J.; Hong, M. pH- and Calcium-Dependent Aromatic Network in the SARS-CoV-2 Envelope Protein. *J. Am. Chem. Soc.* **2022**, *144*, 6839–6850.

(48) Elkins, M. R.; Williams, J. K.; Gelenter, M. D.; Dai, P.; Kwon, B.; Sergeyev, I. V.; Pentelute, B. L.; Hong, M. Cholesterol-binding site of the influenza M2 protein in lipid bilayers from solid-state NMR. *Proc. Natl. Acad. Sci. U. S. A.* **2017**, *114*, 12946–12951.

(49) Elkins, M. R.; Sergeyev, I. V.; Hong, M. Determining Cholesterol Binding to Membrane Proteins by Cholesterol 13C Labeling in Yeast and Dynamic Nuclear Polarization NMR. *J. Am. Chem. Soc.* **2018**, *140*, 15437–15449.

(50) Tran, N.; Oh, Y.; Sutherland, M.; Cui, Q.; Hong, M. Cholesterol-Mediated Clustering of the HIV Fusion Protein gp41 in Lipid Bilayers. *J. Mol. Biol.* **2022**, *434*, No. 167345.

(51) Kwon, B.; Mandal, T.; Elkins, M. R.; Oh, Y.; Cui, Q.; Hong, M. Cholesterol Interaction with the Trimeric HIV Fusion Protein gp41 in Lipid Bilayers Investigated by Solid-State NMR Spectroscopy and Molecular Dynamics Simulations. *J. Mol. Biol.* **2020**, *432*, 4705−4721.

(52) Barrett, P. J.; Song, Y.; Van Horn, W. D.; Hustedt, E. J.; Schafer, J. M.; Hadziselimovic, A.; Beel, A. J.; Sanders, C. R. The amyloid precursor protein has a flexible transmembrane domain and binds cholesterol. *Science* **2012**, *336*, 1168−1171.

(53) Hou, G.; Yan, S.; Sun, S.; Han, Y.; Byeon, I. J.; Ahn, J.; Concel, J.; Samoson, A.; Gronenborn, A. M.; Polenova, T. Spin diffusion driven by R-symmetry sequences: applications to homonuclear correlation spectroscopy in MAS NMR of biological and organic solids. *J. Am. Chem. Soc.* **2011**, *133*, 3943−3953.

(54) Roos, M.; Wang, T.; Shcherbakov, A. A.; Hong, M. Fast Magic-Angle-Spinning ^{19}F Spin Exchange NMR for Determining Nanometer ^{19}F-^{19}F Distances in Proteins and Pharmaceutical Compounds. *J. Phys. Chem. B* **2018**, *122*, 2900−2911.

(55) Olender, Z.; Reichert, D.; Müller, A.; Zimmermann, H.; Poupko, R.; Luz, Z. Carbon-13 Chemical-Shift Correlation, Spin Diffusion and Self Diffusion in Isotopically Enriched Tropolone. *J. Magn. Reson., Ser. A* **1996**, *120*, 31−45.

(56) Williams, J. K.; Shcherbakov, A. A.; Wang, J.; Hong, M. Protonation equilibria and pore-opening structure of the dual-histidine influenza B virus M2 transmembrane proton channel from solid-state NMR. *J. Biol. Chem.* **2017**, *292*, 17876−17884.

(57) Xue, K.; Dervisoglu, R.; Sowa, H.; Andreas, L. B. Centerband-Only Detection of Exchange NMR with Natural-Abundance Correction Reveals an Expanded Unit Cell in Phenylalanine Crystals. *ChemPhysChem* **2020**, *21*, 1622−1626.

(58) Takigawa, T.; Ashida, T.; Sasada, Y.; Kakudo, M. The crystal structures of L-tryptophan hydrochloride and hydrobromide. *Bull. Chem. Soc. Jpn.* **1966**, *39*, 2369−2378.

(59) Vanderhart, D. L. Natural-abundance ^{13}C-^{13}C spin exchange in rigid crystalline organic solids. *J. Magn. Reson. (1969)* **1987**, *72*, 13−47.

(60) Lu, J.-X.; Sharpe, S.; Ghirlando, R.; Yau, W.-M.; Tycko, R. Oligomerization state and supramolecular structure of the HIV-1 Vpu protein transmembrane segment in phospholipid bilayers. *Protein Sci.* **2010**, *19*, 1877−1896.

(61) Clarke, D.; Griffin, S.; Beales, L.; Gelais, C. S.; Burgess, S.; Harris, M.; Rowlands, D. Evidence for the formation of a heptameric ion channel complex by the hepatitis C virus p7 protein in vitro. *J. Biol. Chem.* **2006**, *281*, 37057−37068.

(62) Griffin, S. D.; Beales, L. P.; Clarke, D. S.; Worsfold, O.; Evans, S. D.; Jaeger, J.; Harris, M. P.; Rowlands, D. J. The p7 protein of hepatitis C virus forms an ion channel that is blocked by the antiviral drug, Amantadine. *FEBS Lett.* **2003**, *535*, 34−38.

(63) Montserret, R.; Saint, N.; Vanbelle, C.; Salvay, A. G.; Simorre, J. P.; Ebel, C.; Sapay, N.; Renisio, J. G.; Böckmann, A.; Steinmann, E.; Pietschmann, T.; Dubuisson, J.; Chipot, C.; Penin, F. NMR structure and ion channel activity of the p7 protein from hepatitis C virus. *J. Biol. Chem.* **2010**, *285*, 31446−31461.

(64) Luik, P.; Chew, C.; Aittoniemi, J.; Chang, J.; Wentworth, P., Jr.; Dwek, R. A.; Biggin, P. C.; Vénien-Bryan, C.; Zitzmann, N. The 3-dimensional structure of a hepatitis C virus p7 ion channel by electron microscopy. *Proc. Natl. Acad. Sci. U. S. A.* **2009**, *106*, 12712−12716.

(65) Visscher, K. M.; Medeiros-Silva, J.; Mance, D.; Rodrigues, J.; Daniëls, M.; Bonvin, A.; Baldus, M.; Weingarth, M. Supramolecular Organization and Functional Implications of K$^+$ Channel Clusters in Membranes. *Angew. Chem. Int. Ed.* **2017**, *56*, 13222−13227.

(66) Navedo, M. F.; Cheng, E. P.; Yuan, C.; Votaw, S.; Molkentin, J. D.; Scott, J. D.; Santana, L. F. Increased coupled gating of L-type Ca2+ channels during hypertension and Timothy syndrome. *Circ. Res.* **2010**, *106*, 748−756.

(67) Lim, S. T.; Antonucci, D. E.; Scannevin, R. H.; Trimmer, J. S. A novel targeting signal for proximal clustering of the Kv2.1 K$^+$ channel in hippocampal neurons. *Neuron* **2000**, *25*, 385−397.

(68) Sutherland, M.; Tran, N.; Hong, M. Clustering of tetrameric influenza M2 peptides in lipid bilayers investigated by ^{19}F solid-state NMR. *Biochim. Biophys. Acta, Biomembr.* **2022**, *1864*, No. 183909.

(69) Paulino, J.; Pang, X.; Hung, I.; Zhou, H. X.; Cross, T. A. Influenza A M2 Channel Clustering at High Protein/Lipid Ratios: Viral Budding Implications. *Biophys. J.* **2019**, *116*, 1075−1084.

(70) Raamsman, M. J.; Locker, J. K.; de Hooge, A.; de Vries, A. A.; Griffiths, G.; Vennema, H.; Rottier, P. J. Characterization of the coronavirus mouse hepatitis virus strain A59 small membrane protein E. *J. Virol.* **2000**, *74*, 2333−2342.

(71) Boson, B.; Legros, V.; Zhou, B.; Siret, E.; Mathieu, C.; Cosset, F. L.; Lavillette, D.; Denolly, S. The SARS-CoV-2 envelope and membrane proteins modulate maturation and retention of the spike protein, allowing assembly of virus-like particles. *J. Biol. Chem.* **2021**, *296*, 100111.

(72) Nal, B.; Chan, C.; Kien, F.; Siu, L.; Tse, J.; Chu, K.; Kam, J.; Staropoli, I.; Crescenzo-Chaigne, B.; Escriou, N.; van der Werf, S.; Yuen, K. Y.; Altmeyer, R. Differential maturation and subcellular localization of severe acute respiratory syndrome coronavirus surface proteins S, M and E. *J. Gen. Virol.* **2005**, *86*, 1423−1434.

(73) Wang, Y. H.; Collins, A.; Guo, L.; Smith-Dupont, K. B.; Gai, F.; Svitkina, T.; Janmey, P. A. Divalent cation-induced cluster formation by polyphosphoinositides in model membranes. *J. Am. Chem. Soc.* **2012**, *134*, 3387−3395.

(74) Khuong, T. M.; Habets, R. L.; Kuenen, S.; Witkowska, A.; Kasprowicz, J.; Swerts, J.; Jahn, R.; van den Bogaart, G.; Verstreken, P. Synaptic PI(3,4,5)P3 is required for Syntaxin1A clustering and neurotransmitter release. *Neuron* **2013**, *77*, 1097−1108.

(75) James, D. J.; Khodthong, C.; Kowalchyk, J. A.; Martin, T. F. Phosphatidylinositol 4,5-bisphosphate regulates SNARE-dependent membrane fusion. *J. Cell Biol.* **2008**, *182*, 355−366.

(76) Honigmann, A.; van den Bogaart, G.; Iraheta, E.; Risselada, H. J.; Milovanovic, D.; Mueller, V.; Müllar, S.; Diederichsen, U.; Fasshauer, D.; Grubmüller, H.; Hell, S. W.; Eggeling, C.; Kühnel, K.; Jahn, R. Phosphatidylinositol 4,5-bisphosphate clusters act as molecular beacons for vesicle recruitment. *Nat. Struct. Mol. Biol.* **2013**, *20*, 679−686.

(77) Aleshin, A. E.; Yao, Y.; Iftikhar, A.; Bobkov, A. A.; Yu, J.; Cadwell, G.; Klein, M. G.; Dong, C.; Bankston, L. A.; Liddington, R. C.; Im, W.; Powis, G.; Marassi, F. M. Structural basis for the association of PLEKHA7 with membrane-embedded phosphatidyli-nositol lipids. *Structure* **2021**, *29*, 1029−1039.e3.

(78) Graber, Z. T.; Shi, Z.; Baumgart, T. Cations induce shape remodeling of negatively charged phospholipid membranes. *Phys. Chem. Chem. Phys.* **2017**, *19*, 15285−15295.

(79) Boettcher, J. M.; Davis-Harrison, R. L.; Clay, M. C.; Nieuwkoop, A. J.; Ohkubo, Y. Z.; Tajkhorshid, E.; Morrissey, J. H.; Rienstra, C. M. Atomic view of calcium-induced clustering of phosphatidylserine in mixed lipid bilayers. *Biochemistry* **2011**, *50*, 2264−2273.

(80) Mandala, V. S.; Liao, S. Y.; Kwon, B.; Hong, M. Structural Basis for Asymmetric Conductance of the Influenza M2 Proton Channel Investigated by Solid-State NMR Spectroscopy. *J. Mol. Biol.* **2017**, *429*, 2192−2210.

(81) Hu, F.; Luo, W.; Hong, M. Mechanisms of proton conduction and gating in influenza M2 proton channels from solid-state NMR. *Science* **2010**, *330*, 505−508.

(82) Pinto, L. H.; Dieckmann, G. R.; Gandhi, C. S.; Papworth, C. G.; Braman, J.; Shaughnessy, M. A.; Lear, J. D.; Lamb, R. A.; DeGrado, W. F. A functionally defined model for the M2 proton channel of influenza A virus suggests a mechanism for its ion selectivity. *Proc. Natl. Acad. Sci. U. S. A.* **1997**, *94*, 11301−11306.

(83) Tang, Y.; Zaitseva, F.; Lamb, R. A.; Pinto, L. H. The gate of the influenza virus M2 proton channel is formed by a single tryptophan residue. *J. Biol. Chem.* **2002**, *277*, 39880−39886.

(84) Williams, J. K.; Tietze, D.; Lee, M.; Wang, J.; Hong, M. Solid-State NMR Investigation of the Conformation, Proton Conduction, and Hydration of the Influenza B Virus M2 Transmembrane Proton Channel. *J. Am. Chem. Soc.* **2016**, *138*, 8143−8155.

(85) StGelais, C.; Foster, T. L.; Verow, M.; Atkins, E.; Fishwick, C. W.; Rowlands, D.; Harris, M.; Griffin, S. Determinants of hepatitis C virus p7 ion channel function and drug sensitivity identified in vitro. *J. Virol.* **2009**, *83*, 7970−7981.

📖 Recommended by ACS

Supplementary Information

The SARS-CoV-2 Envelope Protein Forms Clustered Pentamers in Lipid Bilayers

Noah H. Somberg [1], Westley W. Wu [1], João Medeiros-Silva [1], Aurelio J. Dregni [1], Hyunil Jo [2], William F. DeGrado [2] and Mei Hong [1]*

[1] Department of Chemistry, Massachusetts Institute of Technology, 170 Albany Street, Cambridge, MA 02139

[2] Department of Pharmaceutical Chemistry, 555 Mission Bay Blvd. South, University of California, San Francisco, San Francisco, CA 94158

* Corresponding author: Professor Mei Hong, meihong@mit.edu

Calculation of the overlap integral F(0).

The rate constant, k_{ij} for ^{1}H-driven spin diffusion is given by:

$$k_{ij} = \frac{1}{2}\pi\omega_{ij}^2 F_{ij}(0) \tag{1}$$

where ω_{ij} is the homonuclear dipolar coupling:

$$\omega_{ij} = \frac{\mu_0 \hbar}{4\pi}\gamma^2 \frac{1}{r_{ij}^3}\frac{(1-3\cos^2\theta_{ij})}{2} \tag{2}$$

The homonuclear dipolar coupling depends on the internuclear distance r_{ij} and the angle θ_{ij} between the internuclear vector and the external magnetic field. $F_{ij}(0)$ is the overlap integral describing the probability that single-quantum transitions occur at the same frequency for spins i and j.

Spin diffusion among n spins can be calculated from the time-evolution of of the n-by-1 vector of z-magnetization M and the n-by-n exchange matrix $\widehat{K}$. The time evolution is given by:

$$\frac{d\vec{M}(t)}{dt} = -\widehat{K}\vec{M}(t) \tag{3}$$

For an n spin system, the exchange matrix is given by:

$$\widehat{K} = \begin{bmatrix} k_{ab}+k_{ac}+\cdots+k_{an} & -k_{ba} & -k_{ca} & \cdots & -k_{na} \\ -k_{ab} & k_{ba}+k_{bc}+\cdots+k_{bn} & -k_{cb} & \cdots & -k_{nb} \\ -k_{ac} & -k_{bc} & k_{ca}+k_{cb}+\cdots+k_{cn} & \cdots & -k_{nc} \\ \vdots & \vdots & \vdots & \ddots & \vdots \\ -k_{an} & -k_{bn} & -k_{cn} & \cdots & k_{na}+k_{nb}+k_{nc}+\cdots \end{bmatrix} \tag{4}$$

Detailed balance requires that rate constants satisfy $k_{ab} = k_{ba}$, giving a symmetric matrix. Conservation of magnetization then requires that each column sums to zero. The case for a 2-spin system is highly tractable, and worth solving directly. Taking the two-spin system, we have $k_{ab} = k_{ba} = k$, giving the 2 x 2 exchange matrix:

$$\widehat{K} = \begin{bmatrix} k & -k \\ -k & k \end{bmatrix} \tag{5}$$

Let A and B be the z magnetization on spins A and B at time t. Our differential equation is:

$$\frac{d\vec{M}(t)}{dt} = \begin{bmatrix} \dot{A} \\ \dot{B} \end{bmatrix} = \begin{bmatrix} -k & k \\ k & -k \end{bmatrix}\begin{bmatrix} A \\ B \end{bmatrix} \tag{6}$$

The matrix $-\widehat{K}$ has Trace $-2k$ and Determinant 0. The eigenvalues then are $\lambda_1 = 0$ and $\lambda_2 = -2k$, corresponding to eigenvectors $[1, 1]$ and $[1, -1]$ respectively. The general solution is then:

$$\begin{bmatrix} A \\ B \end{bmatrix} = c_1 \begin{bmatrix} 1 \\ 1 \end{bmatrix} + c_2 e^{-2kt} \begin{bmatrix} 1 \\ -1 \end{bmatrix} \tag{7}$$

Imposing the initial condition [1, 0] gives the solution

$$\begin{bmatrix} A \\ B \end{bmatrix} = 0.5 \begin{bmatrix} 1 \\ 1 \end{bmatrix} + 0.5 e^{-2kt} \begin{bmatrix} 1 \\ -1 \end{bmatrix} \tag{8}$$

The model compound 5-^{19}F-Tryptophan has two orientationally inequivalent spins in the crystal unit cell, and is thus one such system. Fitting experimental data (See **Fig. S3**) to the curve $0.5 + 0.5 e^{-rt}$ gives a best fit r of 183 s^{-1} with $R^2 = 0.9935$. Note this "apparent rate" is twice the magnitude of the [1]H-driven spin diffusion rate constant k_{ij}. L-Tryptophan crystalizes in $P2_1$ space group with two molecules in the unit cell (CSD: 1275812). In the crystal lattice, the nearest neighbor [19]F-^{19}F distance between orientationally inequivalent fluorine atoms is 4.62 Å. A second-moment sum over a 10 Å radius across multiple unit cells gives the effective dipolar coupling, which corresponds to an effective distance of 4.16 Å.

With the fit and the equations above, the overlap integral can be calculated directly.

$$F_{ij}(0) = \frac{2k_{ij}}{\pi <\omega_{ij}^2>} \tag{9}$$

where $<\omega_{ij}^2>$ is the powder-averaged ω_{ij}^2:

$$\omega_{ij}^2 = \left(\frac{\mu_0 \hbar}{4\pi} \gamma^2 \frac{1}{r_{ij}^3} \frac{(1 - 3\cos^2 \theta_{ij})}{2} \right)^2 \tag{10}$$

$$< \omega_{ij}^2 > = \left(\frac{\mu_0 \hbar}{4\pi} \gamma^2 \frac{1}{r_{ij}^3} \right)^2 \frac{1}{4\pi} \int_0^{2\pi} \int_0^{\pi} \left(\frac{(1 - 3\cos^2 \theta_{ij})}{2} \right)^2 \sin \theta \, d\theta d\phi$$
$$= \left(\frac{\mu_0}{4\pi} \gamma^2 \frac{1}{r_{ij}^3} \right)^2 \times \frac{1}{5} \tag{11}$$

The dipolar coupling constant can be calculated directly, or from the [1]H-^{1}H dipolar coupling of $\omega = 120{,}120 \times 2\pi$/s for a 1 Å distance:

$$< \omega_{ij}^2 > = \left(\frac{\mu_0 \hbar}{4\pi} \gamma^2 \frac{1}{r_{ij}^3} \right)^2 \times \frac{1}{5} = \left(120120 \times (0.941)^2 \times \left(\frac{1 \text{Å}}{4.16 \text{ Å}} \right)^3 \times 2\pi/s \right)^2 \times \frac{1}{5}$$
$$= 1.726 \times 10^7 \, rad^2/s^2$$

$$F_{ij}(0) = \frac{2k_{ij}}{\pi <\omega_{ij}^2>} = \frac{183 \, s^{-1}}{\pi \, 1.726 \times 10^7 \, rad^2/s^2} = 3.38 \times 10^{-6} \frac{s}{rad^2} = 3.4 \, \mu s \tag{12}$$
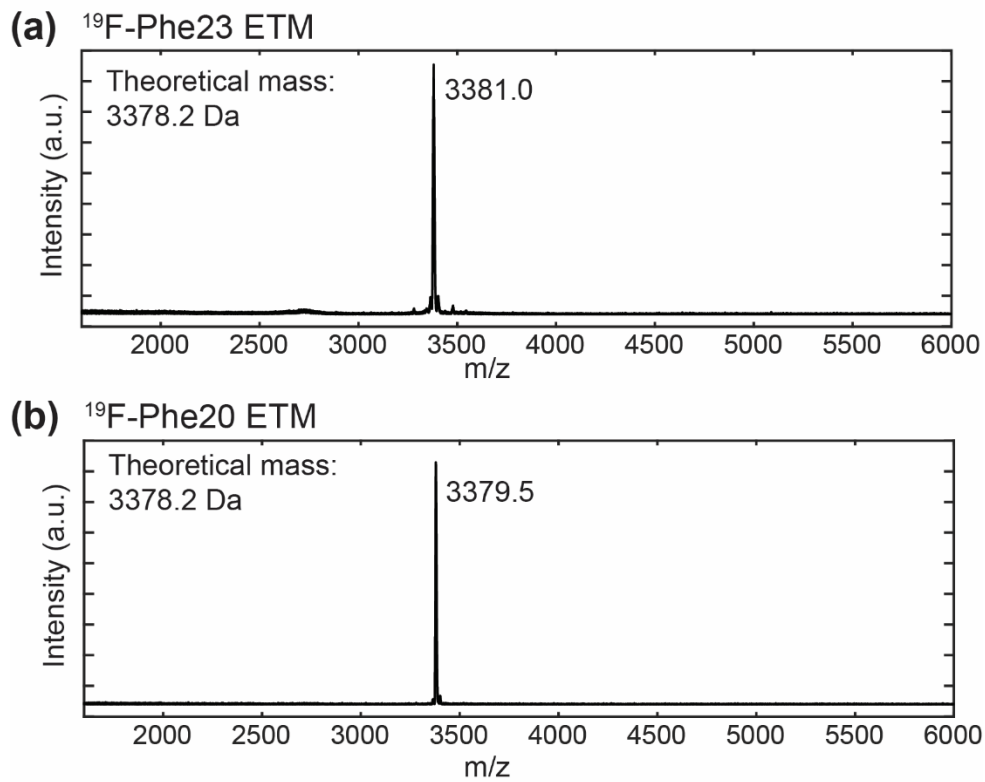
Figure S1 MALDI-TOF mass spectra of synthetic peptides. **(a)** MALDI mass spectrum of synthetic 4[19]F-Phe23 ETM. **(b)** MALDI mass spectrum of synthetic 4[19]F-Phe20 ETM.
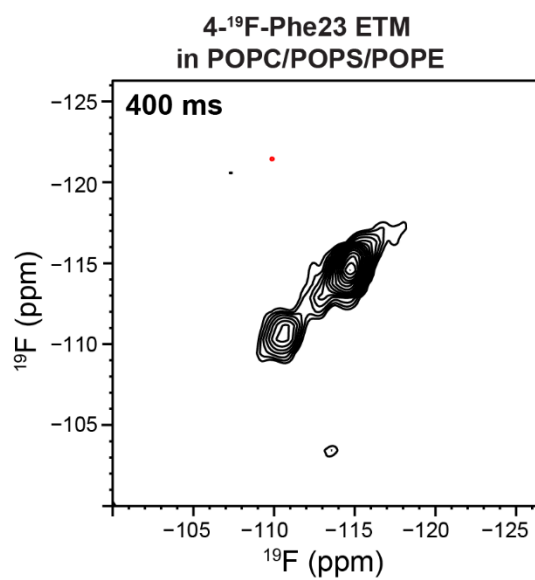
Figure S2. 2D ^{19}F-^{19}F correlation spectra of 4-^{19}F-Phe23 labeled ETM. The spectrum was measured with 400 ms CORD irradiation under 14 kHz MAS at 260 K.
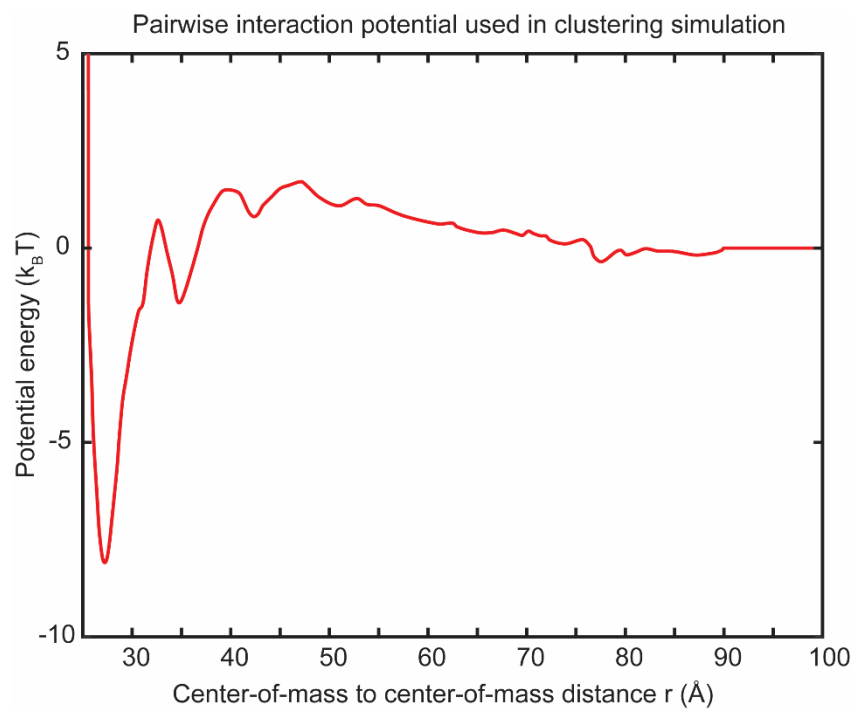
Figure S3. Plot of the pairwise interaction potential used to generate clustered oligomers, reproduced from Morozova et al [1].
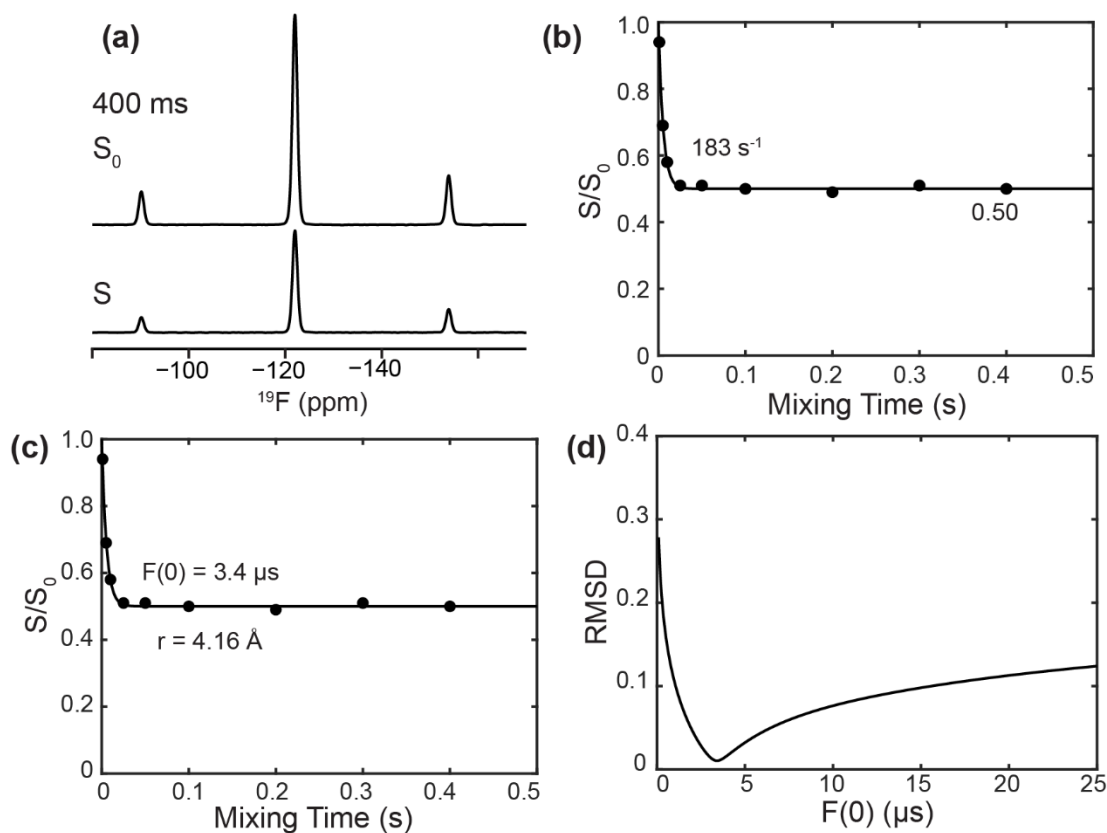
Figure S4. ^{19}F CODEX data of 5-^{19}F-tryptophan, measured under 18 kHz MAS on a 600 MHz NMR, with a ^{19}F Larmor frequency of 564 MHz. (**a**) Representative ^{19}F CODEX S_0 and S spectra, measured at a mixing time of 400 ms. (**b**) Experimental CODEX S/S_0 values (filled circles) superimposed with the best-fit exponential decay (solid line) to 0.5 with the equation $0.5 + 0.5e^{-ct}$, where $c = 183$ s^{-1}. The equilibrium value of 0.50 is consistent with the P2$_1$ space group of L-tryptophan (CSD: 1275812). (**c**) Best-fit matrix simulation of the experimental CODEX intensities. Second moment analysis summing over additional unit cells gives the effective distance of r = 4.16 Å. This results in best-fit overlap integral F(0) of 3.4 µs. (**d**) RMSD between matrix-simulated CODEX decays and the experimental data as a function of F(0) from 0.01 to 25 µs. The best-fit simulation with the lowest RMSD was obtained at F(0) = 3.4 µs.

Reference

1.   Morozova, D.; Weiss, M.; Guigas, G., Shape as a determinant of membrane protein cluster formation. *Soft Matter* **2012,** *8*, 11905-11910.

MATLAB code for matrix calculation of CODEX decay curves

```matlab
%--------------------------------------------------------------------------%
% CODEX_calc.m
% CODEX matrix calculation for a regular polygon of n spins
% Noah H. Somberg, Westley W. Wu, Mei Hong
% Written in MATLAB R2021b
% July 2022
% This script takes a distance matrix (which here is generated based on a
% regular polygon) and calculates a time-dependent CODEX decay using
% 1H-driven spin diffusion theory, and plots the results
%--------------------------------------------------------------------------%

%--------SIMULATION PARAMETERS--------%
gamma = 251.185e6; % Gyromagnetic ratio of fluorine
mu_0 = 1.25663706212e-6; % Vacuum permeability
hbar = 1.054571817e-34; % Planck constant
gammaProt = 267.52218744e6; % Proton gyro ratio
ang = 1e-10; % One angstrom
powd = 0.2; % Powder average of angular dependence

uplimit = 5000; % Upper bound of CODEX plot in ms (x axis)
step = 1; % Time increment in ms (smaller equals smoother curves)

n = 5; % Oligomer number
%s = 8; % Nearest neighbor distance

time_ax = 0:step:uplimit;
F0 = 3.4; % Overlap integra
s = 8.8; % NN distance in A

% Create a polygon with n sides of length n at [0,0] with initial rotation
% 0 degrees
poly = createPoly(n,s,[0;0],0);
dismatrix = zeros(n,n); % Initialize a matrix for all distances


for p1 = 1:n
    for p2 = 1:n % For each set of coordinates
        xdist = abs(poly(1,p2) - poly(1,p1)); % Get x dist
        ydist = abs(poly(2,p2) - poly(2,p1)); % Get y dist
        dismatrix(p1,p2) = sqrt(xdist^2 + ydist^2); % Get total dist
    end
end

% Calculate known couplings to double check parameter values are correct
prot_1a = (mu_0 * hbar * gammaProt^2)/(4*pi*ang^3); % 1A 1H dipolar coup
prot_1a_hz = prot_1a/(2*pi); % Convert to Hz, should be 120120 Hz
```

```matlab
f_1a = (mu_0 * hbar * gamma^2)/(4*pi*ang^3); % 1 A F-F dip coup (in rads!)

dipcoup = f_1a;

M0matrix = eye(n); % Initial state is identity matrix

np=uplimit/step+1; % Number of points

W=dismatrix.^(-3)*dipcoup; % Homonuclear dipolar coupling strength
Wsqu=W.^2; % Coupling squared

for i=1:n % Detailed balance
    Wsqu(i,i)=0; % Zero the diagonal of the coupling matrix
    Wsqu_sums = sum(Wsqu,1); % Sum each column
    Wsqu(i,i) = -Wsqu_sums(i); % Diag set to neg sum
end

% Calculate the exchange matrix K
K=0.5*pi*Wsqu*powd*F0/1000000;
% Mt is a 3d matrix:
% first axis is the ending spin,
% second axis is starting spin,
% 3rd axis is time
Mt = zeros(n,n,np);
prop = expm(step/1000*K); % Calculate the propagator

for currSpin = 1:n
    % For each spin,
    % calc the dip coup matrix W and the dip coup square

    M0 = M0matrix(:,currSpin); % Extract the vector for init mag on spin
    currMat = expm(0/1000*K); % Calculate the initial SD matrix

    t_idx = 1; % Initialize a time index

    for t = 0:step:uplimit
        % For each time step, calculate exchange process
        Mt(currSpin,:,t_idx) = currMat*M0; % Calculate Mt
        currMat = prop*currMat; % Increment exchange matrix

        t_idx = t_idx + 1; % Increment time index
    end
end

Mt_avg = zeros(2,np); % Initialize a matrix for avg magnetization
Mt_avg(1,:) = 0:step:uplimit; % First row is time, second row is M(t) avg

% Calculate average over all spins
for t_idx = 1:np
    % Calc avg mag at each time pt
```

```matlab
        Mt_avg(2,t_idx) = trace(Mt(:,:,t_idx))/n;
end

sim = Mt_avg(2,:);

% Plot the result
figure;
set(gca, 'FontName', 'Arial')
hold on
plot(time_ax./1000,sim,'k','LineWidth',2)
xlim([0,5]);
ylim([0, 1.1]);
xticks([0:1:5]);
yticks([0:0.2:1]);
box on
set(gca, 'FontName', 'Arial')
set(gca,'FontSize',16)
set(gca,'linewidth',2)

function points = createPoly(n,s,origin,rot)
    % Outputs a set of points forming a regular polygon with n sides of
    % length s centered at origin, with an initial rotation with respect to
    % the x axis of rot

    theta = 360/n; % Angle for drawing polygon radial vectors
    points = zeros(2,n); % Initialize output matrix
    Rotmat = [cosd(theta), -sind(theta); sind(theta), cosd(theta)];
    % Length of first vector based on side, using law of cosines
    veclen = sqrt(s^2/(2-2*cosd(theta)));

    xtran = origin(1);
    ytran = origin(2);

    % Get first vertex from length of radial vector and initial inclination
    % angle
    points(:,1) = [veclen*cosd(rot); veclen*sind(rot)];

    % Calculate remaining points by applying rotation matrix
    for i = 2:n
        points(:,i) = Rotmat*points(:,i-1);
    end

    % Translate the shape to the specified origin
    points(1,:) = points(1,:)+xtran;
    points(2,:) = points(2,:)+ytran;
end

%-----------------------------------------------------------------------%
% End of CODEX_calc.m
%-----------------------------------------------------------------------%
```

MATLAB code for simulating a Random Sequential Adsorption of oligomers to a square

```matlab
%----------------------------------------------------------------------------%
% RSAsimulation.m
% Random sequential adsorption of pores
% Westley W. Wu, Noah H. Somberg, Mei Hong
% Written in MATLAB R2021b
% July 2022
% This script takes a specified phospholipid to protein ratio, oligomer
% number, and lipid head group area to place an correspondingly-computed
% number of pores randomly on a 1000 A x 1000 A area, checking for overlap
% with already-placed pores before placing new ones. Outputs the final
% coordinates of the center of each oligomer in
% 'centers_[phospholipid:protein ratio]_[oligomer number].csv'
%----------------------------------------------------------------------------%

% RSAsimulation() places pore centers by randomly adding centers in sequence.
% finalCenters is an output of this function so that other CODEX simulation
% scripts can use the output of this function directly.
function finalCenters = RSAsimulation()
    w = 1000.0; % Width of membrane patch in angstroms
    counter = 0; % Checks how many pores have already been added

    LPRatio = double(input("Lipid:protein ratio: ")); % 10-40
    oligoNum = double(input("Oligomer number: ")); % 4, 5, 6 etc.
    lipidArea = double(input("Area per lipid: ")); % ~60 ang^2
    radius_set = 10; % Radius of the circular footprint of the channel
    % Computes the number of pores
    numPores =
floor((w^2)/(((LPRatio/2.0)*oligoNum*lipidArea)+pi*(double(radius_set)^2)));

    % Initializes array in which the ordered pairs for the final center
    % locations are to be stored
    center_tuples = zeros(numPores, 2);

    while counter < numPores %places the pores sequentially
        x_random = w*rand;
        y_random = w*rand;
        % Checks to see if there is already a pore that could overlap with
        % where we want to place the new pore
        if checkCircle(center_tuples(1:(counter+1),:), x_random, y_random,
radius_set)
            % If there is no overlap, the pore is placed
            center_tuples(counter+1,1) = x_random;
            center_tuples(counter+1,2) = y_random;
            counter = counter + 1;
        end
    end

    finalCenters = center_tuples;
    % Saves the file of pore centers to use later if needed
    writematrix(finalCenters,
strcat('centers_',string(LPRatio),'_',string(oligoNum),'.csv'));
end
```

```matlab
% yesNo returns true if we can place an oligomer at (x,y) given a list of
% previous pore locations and false if we cannot. oldCenters contains the
% list of ordered pairs of already-placed pores, and r is the radius around
% each oligomer center where there cannot be another oligomer.
function yesNo = checkCircle(oldCenters, x, y, r)
    yesNo = true;
    %vectorized computation of distance from (x, y) to every existing point
    hitPoints = repmat([x y], size(oldCenters,1), 1);
    distances = sqrt(sum(((hitPoints-oldCenters).^2),2));

    for i = 1:size(distances,1) % Cycles through already-placed pores
        if (distances(i,1) <= 2*r) % Verifies center-center distance is OK
            % If even a single overlap occurs, yesNo is set to false and we
            % break out of the function because there is no need to cycle
            % through remaining entries in oldCenters
            yesNo = false;
            break
        end
    end
end

%---------------------------------------------------------------------------%
% End of RSAsimulation.m
%---------------------------------------------------------------------------%
```

MATLAB code for Monte Carlo simulation of pore clustering

```matlab
%-------------------------------------------------------------------------%
% ClusteringMonteCarlo.m
% Simulated clustering of oligomers given a pairwise interaction potential
% Westley W. Wu, Noah H. Somberg, Mei Hong
% Written in MATLAB R2021b
% July 2022
% This script takes a specified number of pores and places them randomly on
% a 1000 A x 1000 A area. It then applies the interaction potential and
% simulates with a Metropolis Monte Carlo method. The interaction potential
% is read from the file 'interaction_potential.txt'. This simulation uses
% periodic boundary conditions and outputs the final coordinates of the
% center of each oligomer in 'finalCenters.csv'
%-------------------------------------------------------------------------%

%%%%%%% Begin main program %%%%%%%

%%% Initialize a random list of ordered pairs to serve as an initial random
%%% distribution of pores

% How many pores we place — for 1:17 P:L ratio in a 1000 A x 1000 A box,
% 349 pores are appropriate
npores = 349;
% Generates a membrane patch with 1:17 P:L ratio given the number of pores
sl = sqrt(1000000*(npores/349));
% Initial pore center locations are created. MATLAB randomly picks these
% center coordinates based on the number of pores specified by npores. Note
% that oligomer overlap is allowed
coords = sl*rand(npores,2);
% Saves a record of these initial centers just for future reference
writematrix(coords, 'originalCenters.csv');

% Number of iterations of the Metropolis Monte Carlo algorithm we want to
% simulate. In other words, how many individual oligomer positional changes
% we consider making
ntimes = 50000;

%%% For later plotting of average nearest neighbor (NN) distances

% Average NN distances table: first column will be the iteration the
% simulation is on. The second column will be the NN distance averaged over
% all npores oligomers.
nnVtime = zeros(ntimes+1, 2);
% Computes an average NN distance for the initial pore setup prior to any
% Monte Carlo simulations
nnVtime(1, :) = [0 ANNDistance(coords, sl)];

% For each cycle, we attempt to move a randomly-chosen oligomer to a randomly-
% chosen position. We then use the change in energy between the current and
% proposed configurations to decide if we should accept or reject the proposed
% configuration. Periodic boundary conditions are used.
for i = 1:ntimes
    currentRow = randi(npores); % Chooses a random oligomer to try and move
    % coordsFinal always refers to a proposed state of the system. Here,
```

```matlab
    % we reset the proposed state of the system as the most recently-accepted
    % state at the start of each loop
    coordsFinal = coords;

    % Gets positional information about randomly-chosen point
    current_x = coords(currentRow,1);
    current_y = coords(currentRow,2);

    %computes the energy of initial arrangement
    nearOriginal = nearMe(current_x, current_y, coords, sl); %finds nearest points to
include in an energy calculation of the initial state
    E_i = computeEnergy(coords(currentRow,:), nearOriginal); %actually computes the
energy

    %picks up the point we randomly chose before and moves it to a random
    %location
    finalCoordsForPoint = sl*rand(1,2); %chooses random destination
    coordsFinal(currentRow,:) = finalCoordsForPoint; %changes the position of the
point to the proposed new state

    %gathers positional information about the point's new location
    current_x_f = coordsFinal(currentRow,1);
    current_y_f = coordsFinal(currentRow,2);

    %computes the energy of propsed final state
    nearFinal = nearMe(current_x_f, current_y_f, coordsFinal, sl); %finds nearest
points to include in an energy calculation of the final state
    E_f = computeEnergy(coordsFinal(currentRow,:), nearFinal); %actually computes the
energy

    %decision time: do we accept the new state?
    if E_i-E_f < 0 %if the energy of the proposed state is less favorable than the
energy of the starting state
        if rand <= exp(E_i-E_f) %acceptance criterion
            coords = coordsFinal; %if accept, change system
        end
    else %if the energy of the proposed state is lower, we always accept the proposed
state and work from there next iteration
        coords = coordsFinal;
    end
    nnVtime(i+1, :) = [i ANNDistance(coords, sl)]; %updates NN distance datatable
    disp(i); %displays which iteration we are on, just for reference and can delete
this line if so desired
end

%writes centers of a 3x3 extended grid (to display periodicity)
q1 = [coords(:,1)-sl coords(:,2)+sl];
q2 = [coords(:,1) coords(:,2)+sl];
q3 = [coords(:,1)+sl coords(:,2)+sl];
q4 = [coords(:,1)-sl coords(:,2)];
q5 = coords;
q6 = [coords(:,1)+sl coords(:,2)];
q7 = [coords(:,1)-sl coords(:,2)-sl];
q8 = [coords(:,1) coords(:,2)-sl];
q9 = [coords(:,1)+sl coords(:,2)-sl];
```

```matlab
expandedGrid = [q1;q2;q3;q4;q5;q6;q7;q8;q9];

%saves results
writematrix(expandedGrid, 'expandedFinalCenters.csv'); %saves final pore center
positions with periodic boundary conditions
writematrix(coords, 'finalCenters.csv'); %saves final pore centers w/o periodicity
writematrix(nnVtime, 'avg_NN_dist_v_time.csv'); %saves the time vs average nearest
neighbor data

%figures, for descriptions of figures see their titles

figure(1);
plot(nnVtime(:,1),nnVtime(:,2));
title('Average nearest neighbor distance over time');
xlabel('Timestep');
ylabel('Mean NN distance (angstrom)');
xlim([0 ntimes]);

figure(2);
polygonPoints(5, 8, 0);
xlim([-sl 2*sl]);
ylim([-sl 2*sl]);
title('Final centers');

figure(3);
polygonPoints(5, 8, 1);
xlim([-sl 2*sl]);
ylim([-sl 2*sl]);
title('Original centers');

figure(4);
polygonPoints(5, 8, 2);
xlim([-sl 2*sl]);
ylim([-sl 2*sl]);
title('Final centers w/ periodic boundary conditions');

figure(5);
x = movmean(nnVtime(:,1),500);
y = movmean(nnVtime(:,2),500);
plot(x,y)
title('Average nearest neighbor distance over time');
xlabel('Timestep');
ylabel('Moving average of mean NN distance (angstrom)');


%%%%%%% functions used in main simulation listed below %%%%%%%

function energy = computeEnergy(pt, nearby) %computes the energy of the system
provided a given center location (pt) and a list of its nearest neighbors (nearby)
    %vectorized approach to end up with a list of all distances from the
    %specified point to all the points in the matrix of nearby points
    pointMatrix = repmat(pt, size(nearby,1), 1);
    dist = sqrt(sum(((pointMatrix-nearby).^2),2));

    %computes the energies from distance information
```

```matlab
    if size(dist,1)>=1 %if there are any distances to compute energies from
        dist = double(dist); %converts to double just to be safe
        energies = potential(dist); %runs the distance list through the potential
energy function
        energy = sum(energies,'all'); %adds together all the individual pairwise
energies computed in the line above
    else %if a pore center has no near neighbors, we don't bother computing energy
        energy = 0;
    end
end

function energy = potential(r) %potential function, r is center-center distance in
angstroms
    values = readtable('interaction_potential.txt'); %reads from file
    d = table2array(values(:,1)); %first column contains distances in angstroms
    y = table2array(values(:,2)); %second column contains energies in units of kB*T
    pp = griddedInterpolant(d,y,'makima'); %datafile is a discrete table, uses the
modified Akima interpolation method between discrete points
    energy = pp(double(r)); %computes a numerical value of the energy
end

function expandedGrid = nearMe(x,y,coords,sl) %finds the center coordinates of all
pores at distances close enough to (x,y) such that the pairwise interaction potential
with (x,y) is possibly nonzero
    %initiates 9 copies of the grid in 3x3 arrangement for periodic boundary
conditions
    q1 = [coords(:,1)-sl coords(:,2)+sl];
    q2 = [coords(:,1) coords(:,2)+sl];
    q3 = [coords(:,1)+sl coords(:,2)+sl];
    q4 = [coords(:,1)-sl coords(:,2)];
    q5 = coords;
    q6 = [coords(:,1)+sl coords(:,2)];
    q7 = [coords(:,1)-sl coords(:,2)-sl];
    q8 = [coords(:,1) coords(:,2)-sl];
    q9 = [coords(:,1)+sl coords(:,2)-sl];
    expandedGrid = [q1;q2;q3;q4;q5;q6;q7;q8;q9];
    rowsToRemove = true(size(expandedGrid,1), 1); %by default, remove the entry
unless told otherwise
    same_counter = 0; %keeps track of how many points in expandedGrid have exact
coorindates (x,y); this is only applicable to the extremely unlikely edge case of
different pores having exactly-overlapping centers
    %removes all entries from the expanded periodic set of points outside a
    %200x200 angstrom square centered on (x,y)
    for row = 1:size(expandedGrid,1)
        if (expandedGrid(row,1) == x) && (expandedGrid(row,2) == y) %if the
coordinate is the same as the query point...
            same_counter = same_counter+1; %keep track of it
        end
        if (expandedGrid(row,1) >= x-100) && (expandedGrid(row,1) <= x+100) &&
(expandedGrid(row,2) >= y-100) && (expandedGrid(row,2) <= y+100) &&
(expandedGrid(row,1) ~= x) && (expandedGrid(row,2) ~= y)
            rowsToRemove(row,1) = false; %within the box of interest, so do not
remove entry
        end
    end
```

```matlab
        expandedGrid(rowsToRemove, :) = [];
        temp = repmat([x y], same_counter-1, 1);
        expandedGrid = [expandedGrid; temp];
        %we end up with a list of all pore centers within a 200x200 box of the
        %query point, EXCEPT for the coordinates of the query point itself,
        %since we don't want a nonexistent self-self pairwise interaction
        %contributing to our energy computations.
end

function polygonPoints(n,s,p) %n = oligo number; s = side length; p = centers file to
plot
%plots randomly-angled symmetric pentamers from the centers file generated
%from the Monte Carlo simulation. The code here is ONLY for purposes of
%visualization. the actual pentagon orientations, vertices, and distance
%matrix used in CODEX are generated in our CODEX pentagon-plotting script,
%not here. The output to the entire Monte Carlo simulation is just a file
%of pore centers.
    if  p == 0
        centers = readmatrix("finalCenters.csv"); %filename
    elseif p == 1
        centers = readmatrix("originalCenters.csv"); %filename
    else
        centers = readmatrix("expandedFinalCenters.csv"); %filename
    end
    randi = zeros(1,n); %to be filled with coordinates of the vertices of a regular
n-gon assuming center is (0,0)
    circumradius = (double(s)/2)/(sin(pi/n));
    for j = 1:size(centers,1) %cycles through pore centers, generating a randomly-
angled regular pentagon at each center
        randStart = rand*2*pi/n;
        for i = 1:n
            randi(i) = randStart+2*pi*i/n;
        end
        x_coord = centers(j,1)+circumradius*cos(randi);
        y_coord = centers(j,2)+circumradius*sin(randi);
        patch(x_coord, y_coord, 'blue'); %plots the entire grid of pentagons
    end
end

function dist = ANNDistance(coords, sl) %computes an average nearest neighbor (NN)
distance for given center coordinates (coords) and side length of non-periodic
membrane patch (sl)
    %initiates 9 copies of the grid in 3x3 arrangement for periodic boundary
conditions
    q1 = [coords(:,1)-sl coords(:,2)+sl];
    q2 = [coords(:,1) coords(:,2)+sl];
    q3 = [coords(:,1)+sl coords(:,2)+sl];
    q4 = [coords(:,1)-sl coords(:,2)];
    q5 = coords;
    q6 = [coords(:,1)+sl coords(:,2)];
    q7 = [coords(:,1)-sl coords(:,2)-sl];
    q8 = [coords(:,1) coords(:,2)-sl];
    q9 = [coords(:,1)+sl coords(:,2)-sl];
    expandedGrid = [q1;q2;q3;q4;q5;q6;q7;q8;q9];
    dist = 0; %running sum of NN distances
```

```matlab
    idx = knnsearch(expandedGrid,coords,"K",2);
    for i = 1:size(coords,1) %cycles through each pore in ONLY the non-expanded
grid...
        dist = dist + distance(coords(i,:), expandedGrid(idx(i,2),:)); %...but NN
computations take into account centers that appear as a result of periodic boundary
conditions
    end
    dist = dist/size(coords,1); %computes the actual average by dividing by number of
pores
end

function dist = distance(a, b) %used by many other functions but not directly called
by main program – computes the distance between two ordered pairs a: (a(1), a(2)) and
b: (b(1), b(2))
    dist = sqrt((a(1)-b(1))^2+(a(2)-b(2))^2);
end

%-------------------------------------------------------------------------%
% End of ClusteringMonteCarlo.m
%-------------------------------------------------------------------------%
```

Interaction potential used in the clustering simulation ('interaction_potential.txt')

First column is x-coordinate in angstrom, second column is y-coordinate (energy) in units k_BT

```
-50     10000000.0
0       10000000.0
10      10000000.0
20      10000000.0
25.56605531   -1.351146862
25.72576996   -2.443453329
25.91423324   -3.521822236
26.03881066   -4.623287671
26.41254292   -6.26791972
26.69204355   -7.361819051
27.09771874   -8.060289901
27.50179679   -7.920516088
28.1246839    -6.531936923
28.52876195   -5.469098439
28.68368515   -4.902437082
29.08936034   -3.808537751
29.43114968   -3.305590953
29.77293902   -2.730168844
30.61303804   -1.659764256
31.11134773   -1.403711373
31.51542577   -0.588961453
32.05845556   0.20269194
32.68134267   0.712806626
33.61727048   -0.195524052
34.10440014   -0.704842306
34.59632124   -1.365084422
35.03234222   -1.326059255
36.08965315   -0.50374323
36.68059733   0.031459063
37.2092528    0.551529149
38.08129475   1.055670596
39.35741475   1.490124243
40.10328214   1.490124243
40.78845796   1.428002549
41.94000053   0.884835935
42.34407858   0.807582032
42.74815663   0.869305511
43.24646631   1.089518955
43.96198791   1.272698312
45.14387627   1.552245938
45.8913408    1.614367633
47.13551787   1.707550175
47.69611627   1.606403313
48.94029334   1.311723479
50.99422365   1.086731443
52.86128783   1.272698312
53.79561849   1.125358394
55.07014135   1.086731443
56.75033939   0.900366359
57.68467006   0.815148136
61.01312322   0.621216948
```

```
62.53839806    0.636747372
62.91213033    0.551529149
64.40546224    0.434851864
65.41805308    0.388260593
66.42744962    0.396224912
67.62850374    0.462328767
68.91740091    0.373128385
69.50834509    0.326537114
70.22386669    0.434851864
70.69023345    0.373128385
71.34506349    0.318572794
71.93600767    0.31100669
72.37202864    0.202293724
73.89570634    0.109111182
75.57590438    0.217824148
76.44794634    0.046989487
76.8216786     -0.2166295
77.6298347     -0.348438993
79.54002183    -0.056944887
80.15332606    -0.176011469
81.0525195     -0.109111182
82.04913887    -0.015132208
83.32366172    -0.076855687
84.84893657    -0.084820006
87.0274443     -0.178002549
88.86256555    -0.131411277
89.79689621    -0.053759159
90       0.0
100      0.0
200      0.0
600      0.0
1000     0.0
1500     0.0
```